Heterogeneous integration for on-chip quantum photonic circuits with single quantum dot devices

Marcelo Davanco,[1,*] Jin Liu,[1,2,3,†] Luca Sapienza,[1,4] Chen-Zhao Zhang,[5] José Vinícius De Miranda Cardoso,[1,6] Varun Verma,[7] Richard Mirin,[7] Sae Woo Nam,[7] Liu Liu,[5] and Kartik Srinivasan[1,‡]

[1]*Center for Nanoscale Science and Technology, National Institute of Standards and Technology, Gaithersburg, MD 20899, USA*

[2]*School of Physics, Sun-Yat Sen University, Guangzhou, 510275, China*

[3]*Maryland NanoCenter, University of Maryland, College Park, USA*

[4]*Department of Physics & Astronomy, University of Southampton S017 1BJ, UK*

[5]*South China Academy of Advanced Optoelectronics, Science Building No. 5, South China Normal University, Higher-Education Mega-Center, Guangzhou 510006, China*

[6]*Federal University of Campina Grande, Brazil*

[7]*National Institute of Standards and Technology, Boulder, CO 80305, USA*

(Dated: August 14, 2017)

Abstract

Single quantum emitters are an important resource for photonic quantum technologies, constituting building blocks for single-photon sources, stationary qubits, and deterministic quantum gates. Robust implementation of such functions is achieved through systems that provide both strong light-matter interactions and a low-loss interface between emitters and optical fields. Existing platforms providing such functionality at the single-node level present steep scalability challenges. Here, we develop a heterogeneous photonic integration platform that provides such capabilities in a scalable on-chip implementation, allowing direct integration of GaAs waveguides and cavities containing self-assembled InAs/GaAs quantum dots - a mature class of solid-state quantum emitter - with low-loss Si_3N_4 waveguides. We demonstrate a highly efficient optical interface between Si_3N_4 waveguides and single quantum dots in GaAs geometries, with performance approaching that of devices optimized for each material individually. This includes quantum dot radiative rate enhancement in microcavities, and a path for reaching the non-perturbative strong coupling regime.

Introduction

One of the principal avenues for photonic quantum information processing (QIP) relies on single-photon qubits, with which near-unity fidelity operations can in principle be reached[1]. A tall hurdle towards efficient implementations of single-photon QIP is the difficulty in achieving single-photon nonlinearities for implementing deterministic qubit operations. While measurement-based computation with linear optical networks is a viable alternative[2], the large resource overhead necessary to boost the success rate of non-deterministic gates, and ultimately to significantly scale the size of such systems, is technically very challenging. Indeed, the great level of scalability and stability afforded by photonic integrated circuits has enabled many demonstrations of small-scale quantum computation, simulation, and metrology through this approach[3,4], however scaling such systems towards larger experiments[5] is severely limited by system inefficiencies. In circuits that are, by and large, composed of purely passive elements such as waveguide arrays, phase delays, and beamsplitters, a combination of small photon flux at the circuit input, passive losses in the circuit, and inefficient detection at the output leads to unrealistically long experimental time-scales[6].

In this context, the introduction of solid-state single quantum emitters as functional elements within such photonic circuits can enable significant scaling of on-chip QIP, in two complementary ways. First, by acting as chip-integrated on-demand, bright sources of indistinguishable single-photons, these elements can significantly boost the photonic flux available for interference experiments, thereby enabling the investigation of significantly more complex quantum computing circuits that rely on post-selection[6]. These sources would also enable single-photon level investigation of a variety of physical processes available in chip-based nanophotonic and nanoplasmonic structures, such as Kerr nonlinearities[7] and optomechanical interactions[8]. Secondly, single-emitters strongly coupled to on-chip cavities provide a path towards single-photon nonlinearities[9], and enable deterministic quantum operations through cavity quantum electrodynamics (CQED) within a quantum network formed by a photonic integrated circuit[10].

Towards these goals, we have developed a scalable, integrated, heterogeneous III-V / silicon photonic platform to produce photonic circuits based on Si_3N_4 waveguides that directly incorporate GaAs nanophotonic devices, such as waveguides, ring resonators, and photonic crystals, containing single self-assembled InAs/GaAs quantum dots (QDs). Self-assembled InAs/GaAs QDs in GaAs nanophotonic geometries have been used to demonstrate close-

to-optimal triggered single-photon emission[11,12], spin-qubit operation[13], and a variety of strong-coupling CQED systems[14–16]. Importantly, the ability to produce QDs within high index contrast GaAs nanophotonic geometries has been key in many such demonstrations, enabling control of light-matter interactions through high quality factor, small-mode volume optical resonances. Such coupling enables, for example, efficient channeling of the emitted quantum light into a specific optical mode, large Purcell enhancement, and the achievement of the light-matter strong coupling regime. As a complementary technology, Si_3N_4 waveguides offer low-loss propagation with tailorable dispersion and relatively high Kerr nonlinearities, properties which are currently being explored for linear[17] and nonlinear[7] optical signal processing, as well as cavity optomechanics-based measurements[18], down to the quantum level.

As illustrated in Fig. 1a, our integration platform allows the creation of passive, Si_3N_4 waveguide-based circuits, which can be used for low-loss routing, distribution and interference of light across the chip. At select portions of such passive circuits, GaAs waveguide-based nanophotonic geometries containing self-assembled InAs QDs are produced, on top of a Si_3N_4 waveguide section. As demonstrated below, such active GaAs geometries can be designed to control light-matter interaction between a single embedded InAs/GaAs QD and GaAs-confined propagating waves and localized cavity resonances, while also providing a highly efficient interface between the Si_3N_4 circuit and the QD in the GaAs nanophotonic structure, through adiabatic mode-transformers. To provide the proof-of-principle that such capabilities are achievable, we produce geometries in which QDs inside GaAs waveguides and microring resonators act as sources of single-photons that are launched with high efficiency into Si_3N_4 waveguides. Furthermore, within this platform, we demonstrate effective control of the QD radiative rate by GaAs microring resonators and show the suitability of hybrid microdisks for the achievement of the light-matter strong-coupling regime in this platform.

Our work extends the application space of a mature, scalable, top-down heterogeneous photonic integrated circuit platform[19] into the quantum realm. While several other hybrid/heterogeneous integration technologies are currently being explored (see Supplementary Note 1 for an extended discussion), our work is unique in allowing independent, flexible, and high-resolution tailoring of both active and passive photonic circuit elements with precise and repeatable, sub-50 nm alignment defined strictly by lithography. Taking advantage of the low losses in the Si_3N_4 material, our platform also addresses issues associated with

losses that affect the performance of GaAs-based devices.

Results

Quantum dot interface design While heterogeneous integration of III-V materials for active functionality and silicon-on-insulator for passive functionality has become widespread in classical integrated photonics[19], design considerations for integrated quantum photonics with single quantum emitters are significantly distinct. The first distinction is that, because silicon is opaque at wavelengths below 1 μm, it is a poor material for producing low-loss waveguides that carry light from many important solid-state quantum emitters - such as diamond nitrogen vacancy-centers, single laser dye molecules, epitaxial In(Ga)As/GaAs and GaN quantum dots, colloidal quantum dots, defects in SiC, 2D transition-metal dichalcogenides, hexagonal boron nitride, etc[20]. In our platform, we choose to use stoichiometric silicon nitride, which has a wide transparency window, and can accommodate the full range of In(Ga)As/GaAs quantum dots that have been developed (wavelength ranging from 780 nm to 1300 nm). The second distinction is that strong light-matter interaction requires a sufficiently strong optical field concentration at the emitter location. Such a requirement is considerably relaxed in hybrid, silicon/III-V integrated classical photonic elements such as lasers and amplifiers, because in such devices a reduced degree of light-matter interaction can be offset by the availability of a high density of emitters that interact with the optical field. Indeed, optical confinement in such structures is typically weak, with guided modes that overlap little with the active III-V gain medium[19]. Importantly, due to the weak vertical optical confinement afforded by such geometries, spontaneous emission modal coupling (β) factors are typically considerably less than 100 %, i.e., III-V emitters contribute considerably less than 100 % of their radiation to the interacting, confined optical field. The interacting optical field is, therefore, a poor conveyor of information about any one single emitter. In contrast, in our platform, the large index contrast between the III-V ($n_{\mathrm{GaAs}} \approx 3.5$) and the Si_3N_4 ($n_{\mathrm{Si_3N_4}} \approx 2.0$), can be used to produce optical fields strongly confined in the GaAs material, and which can strongly interact with a single embedded InAs quantum dot (see Supplementary Note 1).

The schematic drawings in Fig. 1b and Fig. 1c respectively show cross-sections of passive and active waveguide sections that form the building blocks of our photonic integration platform. Passive sections consist of Si_3N_4 ridges with SiO_2 and air for bottom and top

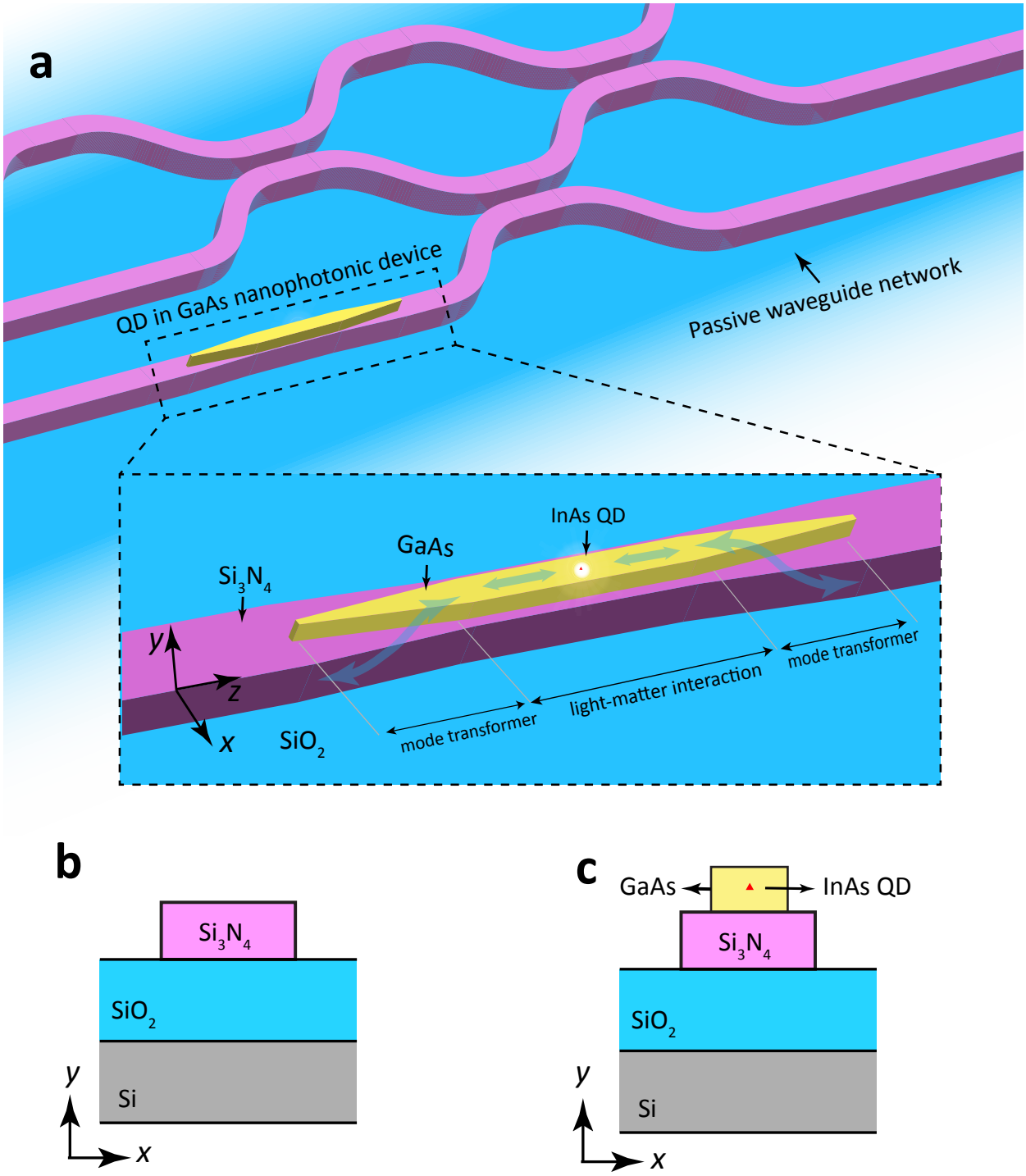

FIG. 1: **Principle of operation and device geometry**. **a**, Conceptual quantum photonic circuit composed of a passive waveguide network with a directly integrated GaAs nanophotonic device (exemplified by a nanowaveguide) containing a single quantum dot. A zoomed-in image of the GaAs device region (inside the dashed boundary box) shows details of the geometry and operation principle of the hybrid photonic integration platform. The light-matter interaction section of the device promotes efficient coupling between a confined electromagnetic field (in this case, a wave confined in a GaAs nanowaveguide) and a single InAs QD embedded in the GaAs. Adiabatic mode transformers allow light from the QD in the light-matter interaction region to be efficiently transferred to a Si_3N_4 waveguide, and, conversely, also allow the QD to be accessed efficiently with resonant light guided by the Si_3N_4 waveguide. **b** and **c**: Cross-sections of passive Si_3N_4 and active

claddings respectively, while active sections consist of the same Si_3N_4 ridge, topped by a GaAs ridge containing a single InAs QD. Active sections are composed of a light-matter interaction geometry (a straight waveguide in the case of Fig. 1a), and adiabatic mode transformer geometries. The light-matter interaction geometry is specifically designed to support guided or localized optical waves that interact strongly with the QD. These can be guided waves of a nano-waveguide, as discussed below, or resonant modes of microring, microdisk or even 1D photonic crystal resonators. The mode transformer geometries, in turn, are designed to efficiently couple the guided or resonant modes of the light-matter interaction geometry to guided modes of the passive Si_3N_4 waveguides.

We illustrate these concepts through an example design of a source of single-photons that are launched directly and with high efficiency into a passive Si_3N_4 waveguide, based on the geometry of Fig. 1a. Here, the light-matter interaction geometry is simply a GaAs waveguide with cross-section in Fig. 1c. The GaAs ridge must support a single transverse-electric (TE) mode, phase-mismatched to the Si_3N_4 guide. This ensures that the fundamental TE supermode of the waveguide stack is strongly concentrated in the GaAs core, as shown in the left panel in Fig. 2a. The InAs QD must then be made to radiate almost exclusively into the fundamental GaAs supermode, rather than into other guided or unbound modes of the stack. The fraction of the total dipole-emitted power that is coupled to the GaAs mode is the β-factor, $0 \leq \beta \leq 1$. $\beta \to 1$ can be achieved for guided modes in waveguides with high refractive index contrasts and sub-wavelength cross-sections, a result of strong field screening inside the guiding core, that takes place for radiative modes[21]. This has been demonstrated in GaAs nanowires or nanowaveguides surrounded by air[22–24] or encapsulated in SiN[25,26]. We predict similar performance for a GaAs nanowire on top of a Si_3N_4 ridge. Assuming a horizontally (x) oriented QD electric dipole moment, we use finite difference time domain (FDTD) simulations to compute β for the GaAs supermode of an active guide designed for emission wavelengths near 1100 nm. The thicknesses of the GaAs and Si_3N_4 layers were taken from the wafer stack used for fabrication (see Methods and Supplementary Note 2). Figure 2b shows a contour map of β as a function of wavelength and GaAs waveguide width, for a Si_3N_4 waveguide thickness of 580 nm and width of 600 nm. For GaAs widths between 300 nm and 400 nm, $0.37 > \beta > 0.35$ for waves traveling in either the $+z$ or $-z$ direction ($0.74 > 2 \cdot \beta > 0.70$ total) is achievable over ≈ 100 nm around 1100 nm. Further simulations (not shown) indicate that β is robust with respect to the Si_3N_4 waveguide width,

to within several tens of nm. Although β is less than the maximum of 0.5 for symmetric emission, we note that both in simulations and in our devices the QD was located at a non-optimal vertical location inside the GaAs. In Supplementary Note 3, we provide similar simulations for an optimized geometry with $\beta > 0.45$ ($2\beta > 0.9$), comparable to those predicted in GaAs nanowires and nanowaveguides[22–24], and in photonic crystal (PhC) slow-light waveguides[27,28]. The mode transformer geometry consists of an adiabatic structure in which the widths of the GaAs and Si_3N_4 waveguides are, respectively, reduced and increased along the z-direction. The width tapers are designed such that the two waveguides become phase-matched over some finite length along the mode converter, where power is efficiently transferred from the GaAs to the Si_3N_4 guide; past the phase-matching length, the taper brings the two guides again away from the phase-matching condition, preventing the power from returning to the top guide. This is illustrated in the middle panel of Fig. 2a, which shows the FDTD simulated electric field distribution for a transformer in which the GaAs and Si_3N_4 widths vary linearly from 300 nm to 100 nm and from 800 nm to 600 nm respectively, over a length of 20 μm. Significantly shorter lengths can potentially be achieved with more sophisticated profiles (see e.g. ref. 29 and references within). Figure 2c shows modal power conversion efficiency from the GaAs mode to the Si_3N_4 mode (right panel of Fig. 2a) as function of wavelength (see Methods for simulation details). Maximum efficiency in excess of 98 % is achieved over a > 200 nm wavelength range. The geometry is robust to variations of tens of nm in the initial and final widths, well within electron-beam lithography tolerances.

Considering these two combined elements, the maximum efficiency of our ideal single-photon source is $\beta \cdot \eta \approx 0.72$ into both directions of the Si_3N_4 waveguide, or 36 % in either the $+z$ or $-z$ direction. For the optimized design in Supplementary Note 3, efficiency > 90 % could potentially be achieved. We note that the source here is symmetric, so emission is in either $\pm z$ direction; unidirectional emission can potentially be implemented with an end-mirror or through chiral coupling[30–32]. We furthermore emphasize that the light-matter interaction geometry can take the form of any waveguide-based geometry, such as 1D photonic crystal cavities, or waveguide-coupled microring or microdisk resonators (see below and Supplementary Note 4 for examples), which may provide high β through Purcell enhancement. In microring or microdisk resonator geometries, a GaAs bus waveguide must be used to evanescently couple to whispering-gallery modes; the bus waveguide can in turn be efficiently coupled to an underlying Si_3N_4 waveguide through mode transformers, as

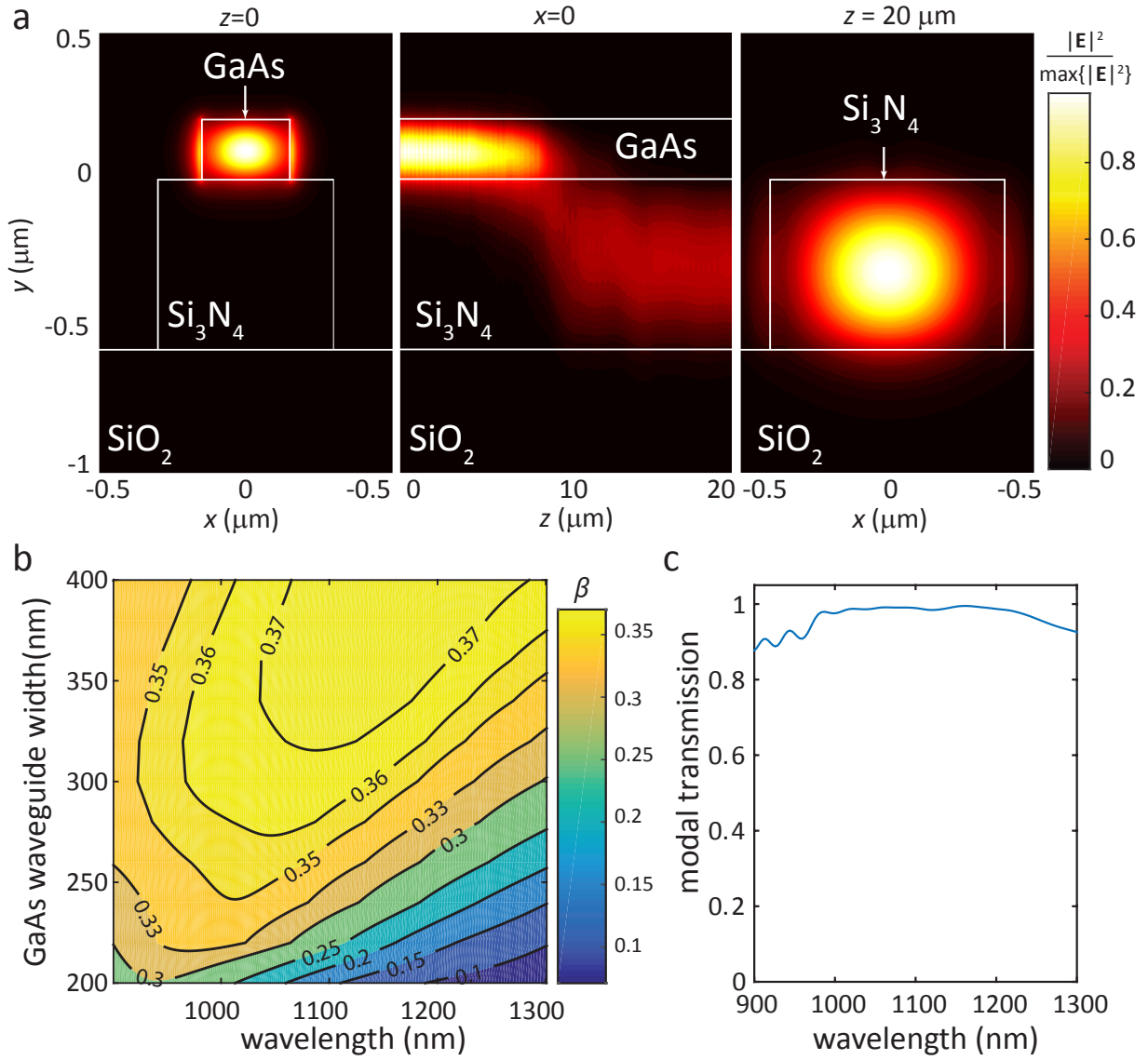

FIG. 2: **Nanophotonic design**. **a**, Left panel: Electric field distribution for the fundamental TE GaAs supermode of the waveguide stack in Fig. 1c, with dimensions specified in the main text. Center panel: Electric field distribution across the mode-transformer cross-section, for a GaAs mode launched at $z = 0$. At $z \approx 10\,\mu$m, the GaAs and Si_3N_4 guides are phase-matched, and power is efficiently transferred from the top GaAs to the bottom Si_3N_4 guide. Right panel: Fundamental TE mode of the Si_3N_4 waveguide at the end of the mode transformer. **b**, Coupling efficiency (β), as a function of GaAs width and emission wavelength, of photons emitted by a dipole located at x=0 and 74 nm below the top surface, into the GaAs waveguide mode traveling in either the +z or -z direction. **c**, Modal power conversion efficiency from the GaAs mode into the Si_3N_4 mode in **a**, as a function of wavelength.

demonstrated in the following sections.

Moreover, we predict that our platform may allow the creation of high quality factor ($Q \approx 10^6$) microdisk resonators supporting whispering-gallery modes with volumes of the order of a few cubic wavelengths (see Supplementary Note 4). Such devices would be equivalent to those described in ref. 14, with which the strong-coupling CQED regime was achieved. This suggests that our platform may enable the creation of on-chip networks of strongly-coupled QD-based coherent CQED systems connected by low-loss waveguides, with which on-chip photonic quantum computation going beyond non-deterministic gate operation might be achieved.

We next describe a fabrication process for devices based on the outlined platform, and experimentally demonstrate two types of on-chip single-photon sources.

Heterogenous device integration We start with the wafer stack shown in Fig. 3a. It consists of a silicon substrate topped by a 3 μm thick thermal oxide layer, a 550 nm layer of stoichiometric Si_3N_4, and an epitaxially grown 200 nm GaAs/AlGaAs stack containing a single layer of InAs quantum dots-in-a-well (DWELL)[33] located 74 nm below the top GaAs surface (details Supplementary Note 2). As a result of the self-assembled growth, quantum dots were randomly distributed within this layer, with a density $> 100/\ \mu m^2$. We point out that the devices reported here contain an ensemble of randomly positioned QDs, rather than a single, spatially isolated QD as illustrated in Fig. 1. Nonetheless, the inhomogeneous broadening of the ensemble ensures that the emission from a single QD can be spectrally isolated by selective excitation, allowing proof-of-principle demonstrations of the many capabilities achievable with individual QDs within our platform.

The hybrid III-V semiconductor / Si_3N_4 stack is produced with a low-temperature, oxygen plasma-activated wafer bonding procedure[19] detailed in Supplementary Note 2. Following the wafer bonding step, fabrication proceeds as in Figs. 3b and 3c (optical micrographs of the devices after completion of each step are also shown). An array of Au alignment marks is first produced on top of the GaAs layer via electron-beam lithography followed by metal lift-off. Electron-beam lithography and inductively-coupled plasma etching are next used to define GaAs devices aligned to the Au mark array. After cleanup of the etched sample surface, electron-beam lithography referenced to the same Au mark array is performed to define Si_3N_4 waveguide patterns aligned to the previously etched GaAs devices. Reactive ion etching is then used to produce the Si_3N_4 waveguides. As a final step, the chip is cleaved

perpendicularly to the Si_3N_4 waveguides > 1 mm away from the GaAs devices, to allow access with optical fibers in the endfire configuration. Before cleaving, 168 devices were produced, with a > 80 % overall yield considering just device geometry. Features as small as 50 nm were achieved in the GaAs layer, and alignment accuracy on the order of a few tens of nm between the top and bottom waveguides was typically observed. We point out that, although here we had no control over QD location within the fabricated GaAs devices, we have specifically tailored our fabrication sequence to allow seamless incorporation of positioning techniques capable of spatially mapping QDs with respect to the Au marks[34–36].

Figure 3d is a false-colour scanning electron micrograph (SEM) of a fabricated stacked-waveguide structure, corresponding to the tip of a mode transformer section. GaAs, Si_3N_4 and SiO_2 are coloured in yellow, pink and blue respectively. Figures 3e and 3f show SEMs of two types of fabricated devices, with different emission capture geometries. In Fig. 3e, the capture structure is a straight waveguide as discussed above. The insets show details of the capture and mode transformer sections. In Fig. 3f, the capture structure is a GaAs microring resonator that is evanescently coupled to a bus waveguide with mode transformers, with the same geometry as in Fig. 3e. Here, QD emission coupled to whispering-gallery modes of the GaAs microring are outcoupled through the bus waveguide (coupling region shown in the inset), and then transferred to the Si_3N_4 guide via the mode transformers. We next describe optical measurements done to characterize the photonic performance of the fabricated devices.

Mode transformer characterization Two important parameters common to all types of devices are the mode transformer efficiency η and the external coupling efficiency $\eta_{\,\mathrm{ext}}$. The first determines, together with the β-factor, the efficiency of the interface between the QD-containing GaAs layer and the passive waveguide circuit. The latter is the efficiency with which the device can be accessed from off-chip, ultimately determining the absolute power available for detection.

We estimate the mode transformer η via transmission spectroscopy of a third type of device fabricated within our platform, a waveguide-coupled photonic crystal (PhC) reflector, schematically shown in Fig. 4a. The PhC is a ≈ 300 nm wide GaAs waveguide into which a periodic 1D array of elliptical holes is etched, with lattice constant a. Major and minor hole radii are kept constant over 19 lattice constants at the center, then reduced linearly over 5 constants at the two ends of the array (to minimize radiation losses). The false-colour SEM in

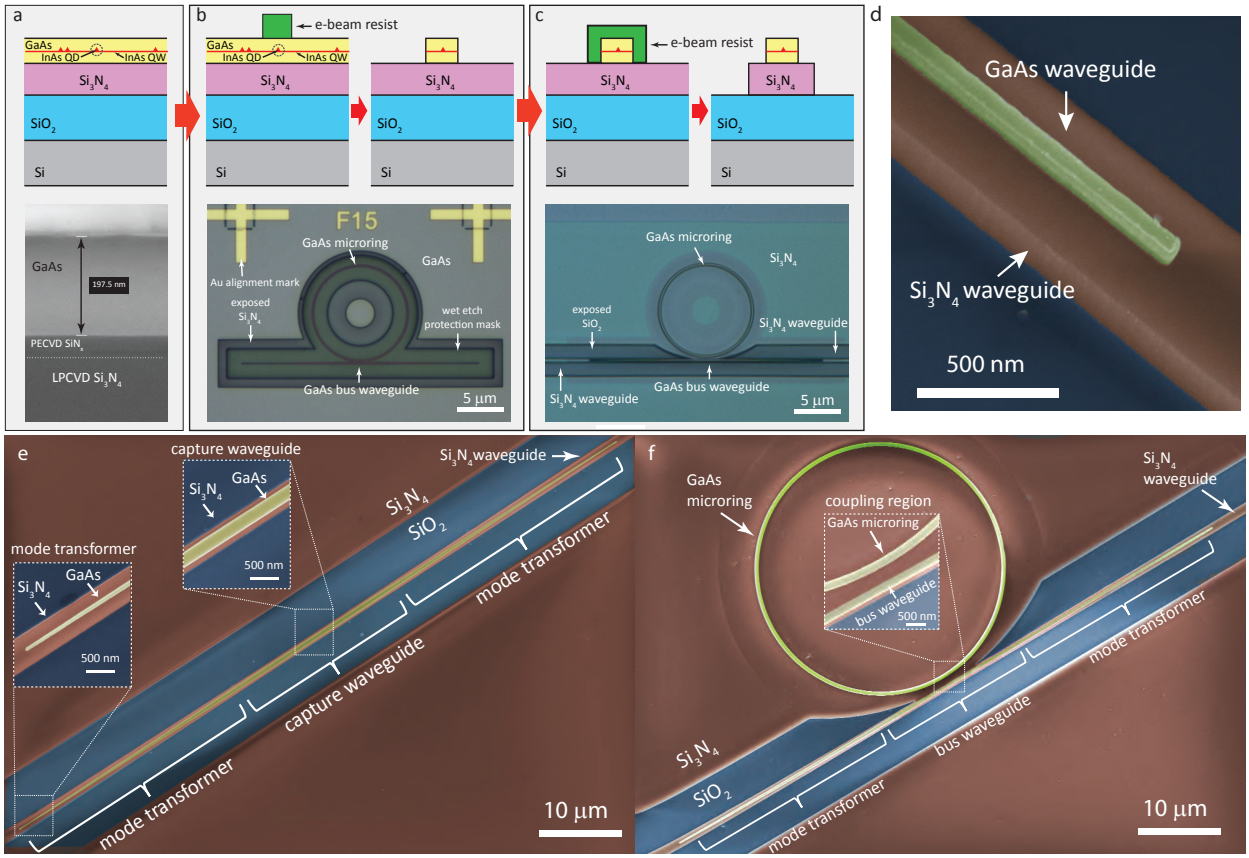

FIG. 3: **Device fabrication**. **a**, Top: schematic of bonded wafer stack used in fabrication, consisting of a top III-V layer, containing InAs QDs, that is directly bonded on top of a Si / 3 μm SiO_2/ 550 nm Si_3N_4 stack. Bottom: cross-sectional scanning electron microgaph (SEM) of bonded wafer stack. The $\approx$ 30 nm SiN_x layer was grown on the GaAs wafer surface prior to bonding. **b**, Top: GaAs device lithography and etching steps. Bottom: optical micrograph of etched GaAs microring resonator and bus waveguide. Au aligment marks used for registered electron-beam lithography are visible. A wet etch protection resist mask (not depicted in the schematic - see Supplementary Note 2) is also visible. **c**, Top: Si_3N_4 waveguide lithography (aligned to the previously etched GaAs device) and etching steps. Bottom: optical micrograph of GaAs microring resonator and bus waveguide, and underlying Si_3N_4 waveguide. **d**, False-colour SEM of tip of mode-transformer geometry, common to both devices in **e** and **f**. **e**, False-colour SEM of fabricated GaAs waveguide (yellow) on top of Si_3N_4 (red) waveguide. Blue regions are exposed SiO_2. Insets show details of the mode transformer end tip and the QD photon capture waveguide. **f**, False-colour SEM of GaAs microring and bus waveguide, and underlying Si_3N_4 waveguide. Inset shows details of the microring-bus waveguide evanescent coupling region.

Fig. 4b illustrates the type of high resolution GaAs devices achievable within our platform. The periodic hole array defines a photonic bandgap for the TE-polarized GaAs mode on the left panel of Fig. 2a, which is strongly reflected by the PhC at bandgap wavelengths. Figure 4a describes the PhC reflector operation. Light is launched into the Si_3N_4 waveguide using a lensed optical fiber aligned to its cleaved facet, then transferred with efficiency η to the GaAs waveguide via the input mode transformer. At bandgap wavelengths, the GaAs-guided light is reflected with reflectivity R by the PhC, then transferred back into the Si_3N_4 waveguide via the input transformer, with efficiency η.

Simulated TE GaAs mode power transmission (T) and reflection (R) spectra are shown in Fig. 4c, for PhCs with $a = 250$ nm and $a = 290$ nm and dimensions estimated by SEM from fabricated devices. Photonic bandgaps are evidenced by high reflectivity, high transmission extinction spectral regions marked in grey. We emphasize that R and T are spectra for the GaAs-confined modes, i.e., they do not include effects due to the mode transformers. We nevertheless observe, in Fig. 4d, similar features experimentally, which suggests spectrally broad mode transformer operation consistent with Fig. 2c. The experimental setup used is described in the Methods and Supplementary Figure 8. Room-temperature characterization is adequate to assess the low-temperature performance given the spectrally broadband nature of the elements involved and the expected thermo-optic shift of GaAs. Figure 4d shows normalized experimental TE-polarized transmission spectra for various fabricated devices with either $a = 250$ nm or $a = 290$ nm. Consistent spectral features achieved across many devices indicate that our photonic integration platform is scalable. Figure 4e shows a typical PhC reflectivity ($R_{\,\mathrm{dev}}$) peak, obtained for one of the $a = 290$ nm devices, spectrally aligned with the transmission extinction region. The > 20 dB (≈ 25 dB at bandgap center) extinction highlighted in grey indicates highly efficient coupling from the Si_3N_4 access waveguide into the GaAs layer, since light not transferred to the GaAs is not reflected by the PhC. As described in the Methods, the photonic bandgap extinction can be used to obtain a lower bound for the mode transformer efficiency η. For a typically observed 20 dB extinction, $\eta > 90$ %, conservatively. For the peak extinction of ≈ 25 dB, $\eta > 94$ %.

To determine the external coupling efficiency $\eta_{\,\mathrm{ext}}$, we took the transmitted power spectrum of a blank Si_3N_4 waveguide (i.e., with no GaAs devices) and normalized it by the supercontinuum source power spectrum. Assuming identical waveguide facets on both chip edges, $\eta_{\,\mathrm{ext}} = 0.23 \pm 0.03$ over the 1100 nm to 1300 nm wavelength range, across three dif-

ferent devices (uncertainties are propagated single standard deviations. See Supplementary Figure 8b for transmission spectra). To verify this, we estimated a mode-mismatch coupling efficiency $\eta_{\text{facet}} \approx 26$ % between the Si_3N_4 waveguide mode and a Gaussian beam with 2.5 μm diameter, consistent with the nominal lensed fiber spot-size diameter. The small difference between the experimental coupling efficiency and the calculated value suggests that propagation losses in the waveguide are relatively small. Indeed, in Supplementary Note 5, propagation losses of ≈ 1.1 dB/cm are estimated from a Si_3N_4 microring resonator transmission spectrum.

Quantum dot coupling to waveguides We next investigated QD emission coupling in our devices via photoluminescence (PL) measurements at cryogenic temperatures. In our setup, shown in Supplementary Figure 5, devices were placed inside a liquid Helium flow cryostat, kept fixed on a copper mount connected to the cold finger. Testing temperatures ranged between 7 K and 30 K. A microscope system allowed individual devices to be visually located and optically pumped with laser light focused through a microscope objective. PL was collected by aligning a lensed fiber (mounted on a xyz nanopositioning stage inside the cryostat) to the corresponding Si_3N_4 waveguide facet. The collected PL was either sent to a grating spectrometer equipped with a liquid nitrogen cooled InGaAs detector array for spectrum measurements, or towards a pair of amorphous WSi superconducting nanowire single-photon detectors (SNSPDs)[37] for time-correlated single photon counting (TCSPC) measurements. We note that the high density QD population in our sample displayed a wide inhomogeneously broadened spectrum, with ensemble s-shell and p-shell peaks located approximately at 1100 nm and 1060 nm respectively.

We first investigated QD emission inside the basic hybrid device, a ≈ 300 nm wide, 10 μm long GaAs waveguide with 20 μm long mode transformers, coupled to a 800 nm wide Si_3N_4 waveguide. Figure 5a shows the PL spectrum collected at a temperature of ≈ 7 K for a device pumped at $\lambda = 1061$ nm (p-shell) with a tunable external-cavity diode laser (ECDL). Sharp spectral lines are excitonic complexes of individual QDs. A ≈ 700 pm full-width at half-maximum (FWHM) bandpass grating filter was used to spectrally isolate the line at 1130.18 nm in Fig. 5a, and a Hanbury-Brown and Twiss (HBT) setup was used to measure the autocorrelation $g^{(2)}(\tau)$, in Figs. 5b and 5c. The values $g^{(2)}(0) = 0.41 \pm 0.13$ obtained for the raw data, and $g^{(2)}(0) = 0 \pm 0.13$ obtained by taking into account the ≈ 129 ps

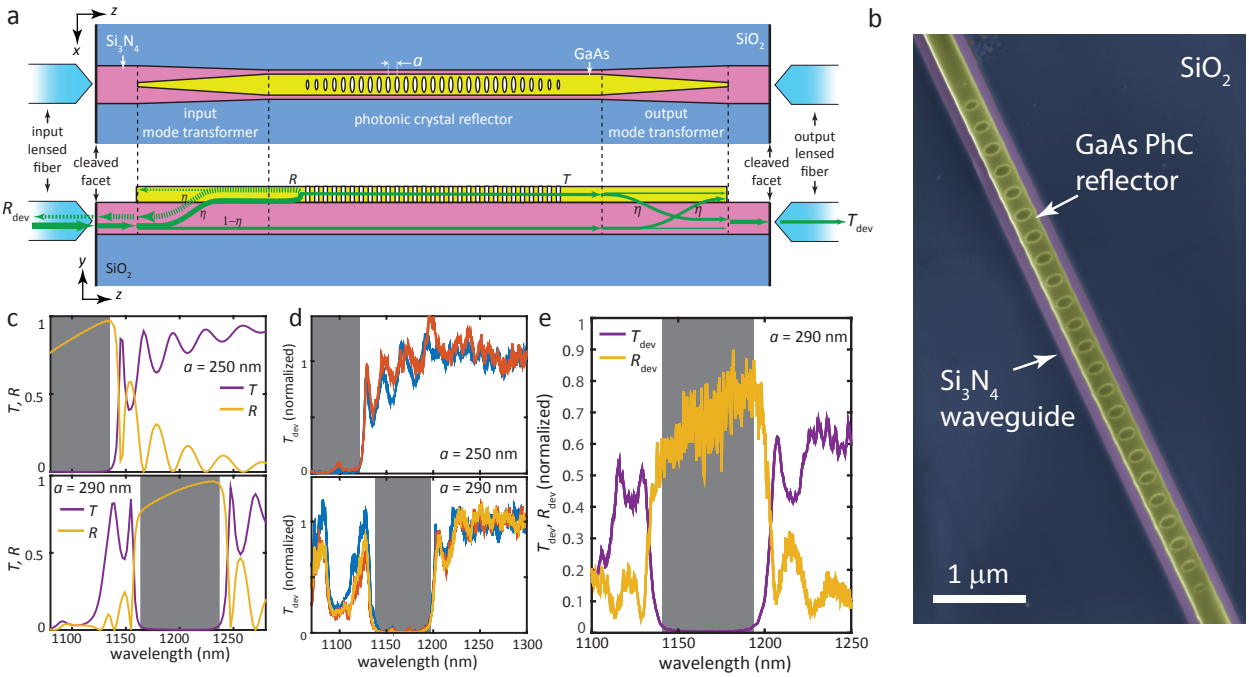

FIG. 4: **Characterizing mode transformer efficiency with a photonic crystal reflector. a**, Schematic of a PhC reflector device. Top: top-view. Bottom: cross-section. Green arrows indicate pathways taken by the optical signal injected at the input port. R and T stand for PhC modal power transmission and reflection spectra, and T_{dev} R_{dev} transmission and reflection spectra through the entire device, including lensed fibers. **b**, False-colour SEM of fabricated GaAs PhC reflector (yellow) on top of a Si_3N_4 (pink) waveguide, on top of exposed SiO_2 (blue). **c**, FDTD-simulated TE modal transmission (T, purple) and reflection (R,yellow) spectra as a function of wavelength for the PhC (without mode transformers), for two different lattice constants a. **d**, Experimental transmission spectra for various PhC reflectors with $a = 250$ nm (top) and $a = 290$ nm (bottom), normalized first by the transmission spectrum of a baseline Si_3N_4 waveguide (without GaAs sections), then to the mean transmission at wavelengths between 1250 nm and 1300 nm. Different colours indicate different devices. **e**, Experimental transmission and reflection spectra for a PhC reflector with $a = 290$ nm, normalized to the transmission spectrum of a baseline Si_3N_4 waveguide. Grey areas have transmission < -15 dB in **c**-**d**, < -20 dB in **e**.

time resolution of our TCSPC system (see Methods), indicate that the QD in the GaAs device acts as source of single-photons that are directly launched into a Si_3N_4 waveguide. $g^{(2)}(0)$ uncertainties quoted here and below are 95 % fit confidence intervals (two standard deviations). Bunching at $\tau \approx \pm 2$ ns suggests QD blinking, as observed with quasi-resonat

(p-shell) excitation in ref. 38, and could be related to coupling of the radiative excited state to dark states. Our fits were done with a function that models coupling of a two-level system to a single dark state[39].

Lifetime measurements for the same QD line were next performed by modulating the ECDL pump light with an electro-optic modulator (see Methods and Supplementary Note 6). The decay curves show in Fig. 5d were fitted with a single exponential function, revealing a lifetime $\tau_{\rm sp} = 1.014$ ns $\pm$ 0.004 ns (lifetime uncertainties here and below are from the fit and correspond to one standard deviation). Assuming a fiber-to-chip coupling efficiency of 22 %, and a coupler efficiency $\eta = 98$ %, we estimate a QD-waveguide coupling parameter $\beta = 0.20 \pm 0.07$ (uncertainty from propagated errors in the optical characterization of the measurement system, corresponding to one standard deviation. See Methods for details). This value, though appreciable, is less than the theoretical maximum of 0.37. This discrepancy could be attributed to non-optimal QD position and electric dipole moment orientation.

Weak-coupling cavity QED We next investigated cavity effects on the radiative rate of single QDs coupled to whispering gallery modes (WGMs) of GaAs microring resonators (Fig. 3f). The devices consisted of 20-μm diameter microrings formed by $\approx$ 300 nm wide waveguides, evanescently coupled to $\approx$ 300 nm wide GaAs bus waveguides spaced by gaps of varying dimensions. In this scheme, light from QDs inside the ring is outcoupled through the bus waveguide and then transferred to the Si_3N_4 waveguide via the mode transformers. Figure 6a shows PL spectra for three different resonators, with coupling gaps of 150 nm, 250 nm and 350 nm, pumped at high intensities with 975 nm laser light (resonant with the quantum well transitions). Peaks are PL from the QD ensemble coupled to WGMs. Quality factors for devices with the gap spacings of 150 nm, 250 nm and 350 nm are 2.5×10^3, 6×10^3 and 2×10^4. The increased Q for larger gaps is due to a decreased cavity-bus waveguide coupling, indicating that the geometrical control afforded by our fabrication platform enables fine control of cavity outcoupling rates. Pumping one of the $Q \approx 1.1 \times 10^4$ microresonators at 1058 nm (p-shell) allowed observation of the single QD excitonic line at 1125.92 nm in Fig. 6b, which was coupled to one of the cavity's WGMs. Background emission, likely from other QDs and (multi)excitonic complexes in the active material, is also observed in the different WGMs. Figure 6c indicates the cavity-coupled QD acts as a single-photon source

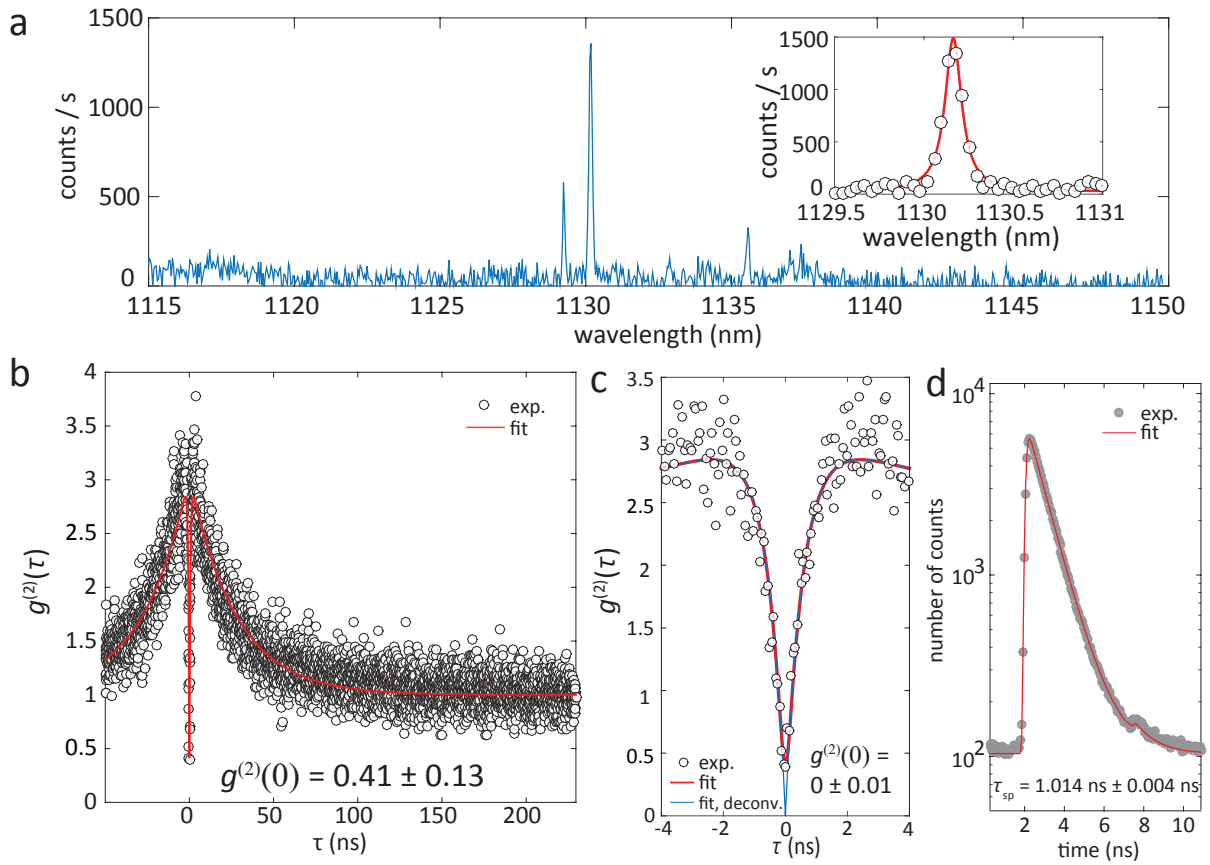

FIG. 5: **Quantum dot-waveguide coupling**. **a**, Photoluminescence spectrum for a single QD inside a GaAs waveguide as in Fig. 3**e**, pumped with 1061 nm wavelength laser light. The PL is transferred to the bottom Si_3N_4 waveguide, and collected with a lensed optical fiber inside of a Liquid Helium flow cryostat (see Supplementary Note 6). Sharp lines are exciton transitions from a single QD. Inset: Fit of PL peak at 1130.18 nm. **b**, Second-order correlation as a function of time delay τ for the 1130.18 nm line. Circles mark experimental data, red line is a fit (see Methods and Supplementary Note 7). **c**, Zoom-in of **b** near $\tau = 0$. The blue curve and quoted $g^{(2)}(0)$ are obtained from the red fit by deconvolving the detection time-response. Uncertainties for $g^{(2)}(0)$ are 95 % fit confidence intervals (two standard deviations). **d**, Photoluminescence decay trace for the 1130.18 nm line. Gray dots are experimental data, the red line is a fit with a monoexponential function with lifetime τ_{sp}. The uncertainty is obtained from the fit and corresponds to a single standard deviation.

with $g^{(2)}(0) = 0.28 \pm 0.01$ ($g^{(2)}(0) = 0.07 \pm 0.01$ adjusted for detection time resolution).

We next demonstrated tunable control of Purcell radiative rate enhancement in a device with $Q \approx 6 \times 10^3$, at a fixed temperature of ≈ 7 K. Pumping at $\lambda = 1065$ nm (p-shell) allowed us to observe the cavity-mode-coupled single QD exciton line X_1 in Fig. 6d, as well as a cavity-detuned exciton X_2. For the X_1 line, as seen in Fig. 6e, $g^{(2)}(0) = 0.72 \pm 0.08 > 0.5$ ($g^{(2)}(0) = 0.52 \pm 0.08$ adjusted for detection time resolution), due to background emission from the cavity mode, which was transmitted by the band-pass filter introduced before detection. Indeed, based on the fit shown in Fig. 6d, cavity emission corresponds to ≈ 45 % of the filtered light intensity. To tune the cavity with respect to the QD exciton, we used the nitrogen gas-tuning mechanism of ref. 40. A small amount of gaseous N_2 is introduced in steps into the cryostat, and gettering at the GaAs surfaces red-shifts the cavity resonance by a small amount at each step. This is observed in the left panel in Fig. 6f, where the PL spectrum of the cavity-coupled QD exciton (X_1) is seen to grow in intensity as its spectral (wavelength) detuning Δ from the cavity center tends to zero. The variation in intensity comes together with a variation in the exciton lifetime, evident in the corresponding decay curves on the right panel of Fig. 6f. Biexponential fits to the decay data (monoexponential for $\Delta \approx 0.53$ nm and $\Delta \approx 0.84$ nm) are also shown. The detuning-dependent variations in X_1 intensity and decay lifetime are summarized respectively in the left and right panels in Fig. 6g, evidencing high-resolution, strong control of the exciton radiative rate via cavity coupling achieved in our platform. Further details on PL spectrum and decay fitting and assignment of lifetimes are given in Supplementary Note 7. Comparing with the $\approx$1 ns lifetime in the waveguide, we can extract a maximum radiative rate enhancement factor of ≈ 4 for the QD. From the calculated WGM mode volume $V_{\text{eff}} = 75.5(\lambda/n_{\text{GaAs}})^3$ (n_{GaAs} is the GaAs refractive index) and the experimental $Q = 6 \times 10^3$, we expect a maximum Purcell Factor $F_{\text{p}} \approx 6$ (see Methods). Though reasonably close to the theoretical value, the lower experimental Purcell factor could be due to non-optimal spatial location and polarization alignment of the QD with respect to the microring mode.

Discussion

The results presented demonstrate that our platform enables the creation of integrated photonic circuits that incorporate quantum-dot based devices with complex geometries. As discussed above, further improvements to the single-photon capture efficiency (quantified

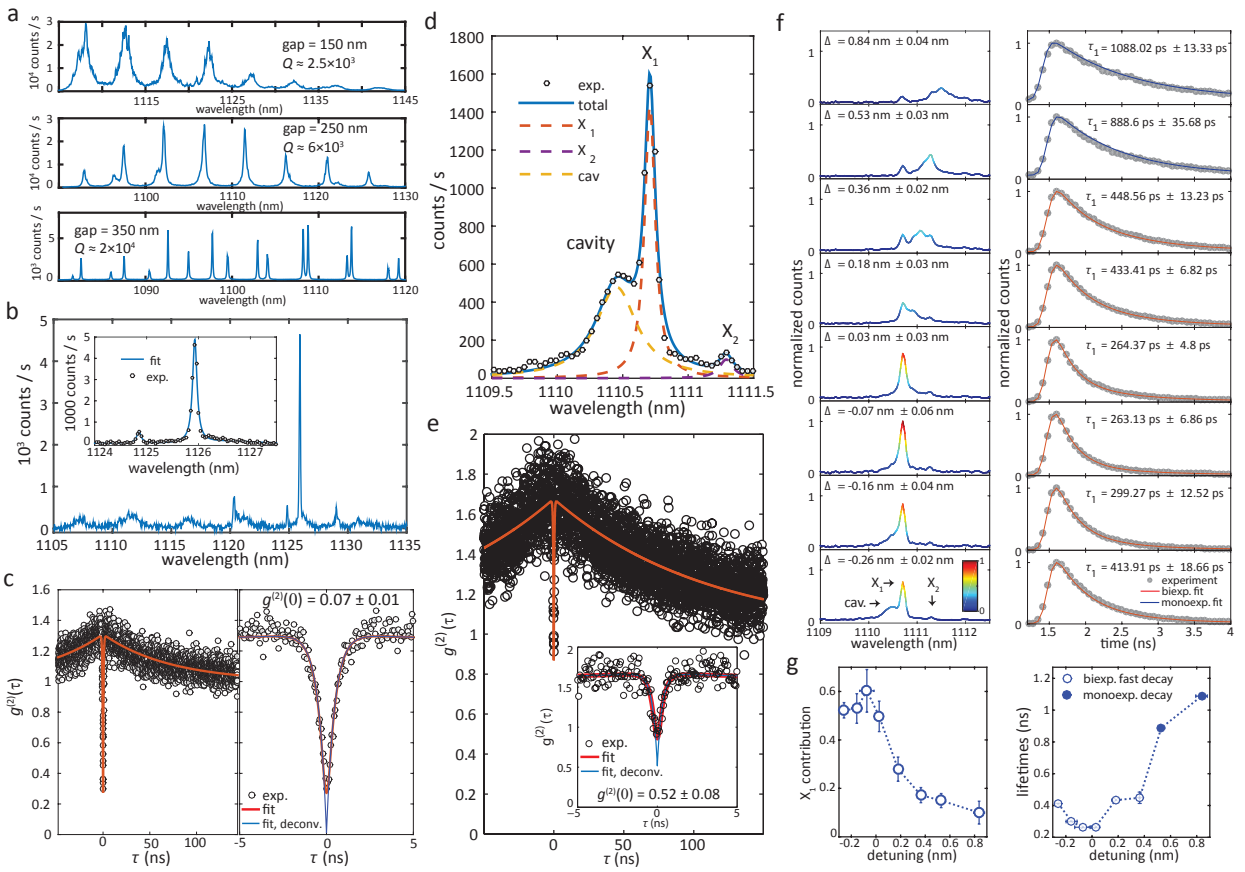

FIG. 6: **Quantum dot-cavity coupling.a**, Photoluminescence (PL) spectra as a function of wavelength from a QD ensemble pumped with laser light at 975 nm, emitting inside three different GaAs microring resonators. Peaks are whispering-gallery modes (WGMs) with quality factor Q, which increases with the microring-bus waveguide gap width. **b**, PL spectrum for a single QD coupled to a $Q \approx 1.1 \times 10^4$ WGM. Inset: fit of cavity-coupled QD emission near 1126 nm. **c**, Left: second-order correlation $g^2(\tau)$ for the 1126 nm exciton line in **b**. Right: close-up near $\tau = 0$. Circles are experimental data, red lines are a fit. The blue curve and quoted $g^{(2)}(0)$ are obtained from the red fit by deconvolving the detection time-response. **d**, PL spectrum for a single QD in a microring, coupled to a $Q \approx 6 \times 10^3$ WGM. Circles: experimental data. Blue continuous line: fit. Dashed lines: fitting Lorentzians for the cavity and two excitons, X_1 and X_2. **e**, $g^2(\tau)$ for X_1 in **d**. Inset: close-up near $\tau = 0$. **f**, Left panel: PL spectra for varying spectral detuning Δ between X_1 and the cavity. Δ is obtained from fits as in **d**. All spectra are normalized to the intensity maximum at $\Delta \approx -0.07$ nm. The colour scale indicates normalized intensity. Right panel: corresponding X_1 photoluminescence decay curves. Grey dots are experimental data, red (blue) lines are biexponential (monoexponential) decay fits. For biexponential fits, τ_1 is the fast lifetime. **g**, Left panel: integrated intensity as a function of Δ for the filtered X_1 exciton contribution to the the PL spectra in **f**, obtained from Lorentzian fits as in **d**, normalized by the integrated intensity of the full fitted spectrum. Right panel: decay lifetimes for the fits in **f**, as a function of Δ. Open blue circles are the fast biexponential decay lifetimes, closed blue circles are the monoexponential decay lifetimes. Uncertainties for $g^{(2)}(0)$, Δ and the X_1 magnitude are 95 % fit confidence intervals (two

by the β-factor) can be achieved through optimized wafer stacks (both Si_3N_4 and the GaAs epi-stack) and device geometries. In particular, our platform allows the creation of geometries providing high Purcell radiative rate enhancement where high β may be achieved, such as microdisk, microcring or photonic crystal-based cavities and slow-light waveguides. The high reflectivity achieved with our PhC reflectors furthermore suggests a path forward towards unidirectional QD emission in a waveguide. Alternatively, chiral coupling to waveguide modes[30] could also be explored. Strongly-coupled QD-cavity systems[14–16] evanescently coupled to a bus waveguide could also be envisioned in our platform.

As mentioned above, our III-V wafers contained a high density of QDs ($> 100/\,\mu m^2$), randomly distributed across the wafer surface, which led to the deterioration of the purity of our on-chip single-photon sources. It is also possible that the pronounced blinking observed in the autocorrelation traces might stem from interactions between many neighbouring QDs. Low-density QD growth constitutes a clear way forward here. In this case, QD positioning techniques such as the one developed in ref. 34 and 35 -a technique fully compatible with our fabrication process- become essential. Precise quantum dot location within a nanophotonic structure would also allow β and Purcell factor optimization.

The underlying Si_3N_4 waveguides demonstrated here provide not only a way to route single-photons with low loss across the chip, but also a means to explore nonlinear optical processes with single photons. For instance, four-wave-mixing-based wavelength conversion of single-photon-level laser light was recently demonstrated in a Si_3N_4 microring resonator whose cross-sectional dimensions similar to those of our waveguides, and fabricated with the same etch process[7]. This means that the required dispersion profiles and nonlinear coefficients are attainable within our platform. At the same time, passive structures with cross-sections optimized for low propagation losses may also be implemented, for instance with thinner Si_3N_4 (see Supplementary Note 3) and potentially even with a top oxide cladding, which would also enable lower-loss off-chip coupling to optical fibers. The introduction of elements such as on-chip delay lines, high quality Si_3N_4-based filters, and microring add-drops, can also be envisioned.

Our platform is also amenable to further integration with waveguide-based superconducting nanowire single-photon detectors[41]. Finally, the fabrication process can be adapted for materials such as AlN and $LiNbO_3$, which may enable active electro-optic phase control. We anticipate all of these features will enable a new class of monolithic on-chip devices

comprising emission, routing, modulation and detection of quantum light.

Methods

Numerical simulation Calculations of waveguide β-factors is done with finite-difference time-domain simulations. We simulate a x-oriented electric dipole source radiating inside the GaAs ridge of the stacked GaAs/Si_3N_4 waveguide structure shown in Fig. 1c. The simulation is 3D, and the coupled waveguide structure length is 1 μm. Perfectly-matched layers are used to emulate either open regions (air and SiO_2 semi-infinite spaces above and below the geometry), or infinite waveguides (in the planes perpendicular to x and y). We obtain the steady-state electromagnetic fields at the six boundaries of the simulation window, and compute the total emitted power P by integrating the steady-state Poynting vector through them. At the $+z$ and $-z$ planes, we calculate overlap integrals of the radiated field with the field of the fundamental TE GaAs mode (Fig. 2a left panel, at $\lambda = 1100$ nm). This allows us to determine β, the fraction of the total emitted power that is carried through the $\pm z$ planes by the GaAs mode.

The mode transformer simulations are also performed with FDTD. We launch the fundamental TE GaAs mode of the waveguide structure in Fig. 1c, shown in the left panel of Fig. 2a, into the mode transformer, at the $z = 0$ plane. We obtain the steady-state electromagnetic fields at the output ($z = 20$ μm) plane on the mode transformer, and calculate the overlap integral between this and the output Si_3N_4 mode (right panel on Fig. 2a). Dividing it by the launched input power we obtain the mode transformer coupling efficiency η.

We proceed similarly for the simulation of modal reflectivity and transmissivity for the photonic crystal reflector of Fig. 4a. For reflectivity, we place a field monitor at the $z = 0$ plane, and the source at $z = 100$ nm.

To determine the mode volume V_{eff} used in the Purcell factor estimate, we use $V_{\text{eff}} = \int_V dV \epsilon(\mathbf{r}) \left|\mathbf{E}(\mathbf{r})\right|^2 / \max\left\{\epsilon(\mathbf{r}) \left|\mathbf{E}(\mathbf{r})\right|^2\right\}$, where the volume integral is evaluated over the entire microring resonator. Because the ring radius is large ($R = 10\,\mu$m), we assume the whispering gallery mode fields across the microring cross-section have the same distribution as the fundametal TE GaAs mode of Fig. 2a's left panel, and an azimuthal dependence $\exp(i \cdot m\phi)$. Then, $V_{\text{eff}} = 2\pi \cdot R \cdot \int_A dA \epsilon(\mathbf{r}) \left|\mathbf{E}(\mathbf{r})\right|^2 / \max\left\{\epsilon(\mathbf{r}) \left|\mathbf{E}(\mathbf{r})\right|^2\right\}$, where A is the cross-sectional waveguide area. The maximum Purcell factor (assuming spatial and polarization alignment of the dipole) is calculated with the expression $F_{\text{p}} = (3/4\pi^2) \cdot Q/V'_{\text{eff}}$, where V'_{eff} is the mode volume in cubic wavelengths

in the GaAs.

Experimental determination of mode transformer coupling efficiency Power transmission and reflection spectra T_{dev} and R_{dev} are determined experimentally using the setup in Supplementary Figure 8a. Light from a fiber-coupled supercontinuum laser source is passed through a 3 dB fiber directional coupler and polarization controller, then launched into the input waveguide with a lensed fiber. Transmitted light is collected with another lensed fiber aligned to the output waveguide facet at the opposite edge of the chip, and sent to an optical spectrum analyzer (OSA). Reflected light is captured by the input fiber, and routed to the OSA via the 3 dB splitter.

To estimate a lower bound for η, we use a simple model to obtain an expression for the transmitted power at the output, T_{dev}, as suggested in Fig. 4a. Light launched at the input Si_3N_4 waveguide is transferred with efficiency η into the GaAs guide, whereas a residual $(1-\eta)$ portion of the original power remains in the Si_3N_4 guide. Light transferred to the GaAs guide will be reflected with a reflectivity R by the PhC, and transmitted through it with transmissivity T. The output mode transformer converts light transmitted through the PhC reflector back into the Si_3N_4 guide, with efficiency η. We assume that the residual light that remains in the Si_3N_4 after the input mode transformer is unaffected by the PhC, after which it is partially transferred with efficiency η to the GaAs guide by the output mode converter, and is then lost as radiation at the terminated GaAs structure tip. Light collected by the output lensed fiber thus has two components, one that remains in the Si_3N_4 guide, and one that is transferred to and from the GaAs guide, and interacts with the PhC reflector. The maximum power collected by the output lensed fiber is T_{dev}, with

$$T_{\mathrm{dev}} \leq \eta_{\mathrm{ext}} \left[\eta^2 T + (1-\eta)^2 + 2\cdot\eta(1-\eta)\sqrt{T}\right]. \tag{1}$$

Inside the square brackets, the first and second terms correspond respectively to light transmitted through the PhC and residual light that remains in the Si_3N_4 guide, and the third term comes from the interference between the two. The transmitted power for wavelengths in and out of the bandgap region are $T_{\mathrm{dev,in}}$ and $T_{\mathrm{dev,out}}$, respectively, and we define the extinction ratio $\alpha = \frac{T_{\mathrm{dev,in}}}{T_{\mathrm{dev,out}}}$. Because experimentally $T_{\mathrm{dev,in}}$ is at least one order of magnitude lower than $T_{\mathrm{dev,out}}$, we can assume that the PhC transmission at bandgap wavelengths is negligible, so that $T \approx 0$ and

$$\alpha > \frac{(1-\eta)^2}{\eta^2 T + (1-\eta)^2 \pm 2\cdot\eta(1-\eta)\sqrt{T}} > \frac{(1-\eta)^2}{\eta^2 + (1-\eta)^2 + 2\cdot\eta(1-\eta)} \tag{2}$$

Isolating η, we obtain the inequality $\eta^2 + (2-\alpha)/(\alpha-1) + 1 < 0$. The minimum root of the quadratic equation is our lower bound for η. For $\alpha = -20$ dB, as typically observed in our PhC

spectra, $\eta > 90$ %, conservatively. For the peak extinction of ≈ 25 dB, $\eta > 94$ %.

Experimental determination of external coupling efficiency The external coupling efficiency $\eta_{\,\mathrm{ext}}$ includes the chip-to-fiber coupling efficiency and propagation losses in the Si_3N_4 waveguide leading to the device. We employ the setup of Supplementary Figure 8a to obtain the transmitted power spectrum of a blank Si_3N_4 waveguide (i.e., with no GaAs devices). Prior to this measurement, the polarization of the incident light is set to TE by probing a PhC reflector and minimizing the transmitted power over the photonic bandgap with the polarization controller. The lensed fibers are then aligned to the blank Si_3N_4 waveguide, and the transmission spectrum is recorded. The spectrum is then normalized by the supercontinuum source power spectrum, obtained by bypassing the lensed fibers and the device. The resulting transfer function accounts for insertion losses through the two lensed fibers (≈ 31 %), and through the device, $IL_{\,\mathrm{dev}} = \eta_{\,\mathrm{dev}}^{-1} = (\eta_{\mathrm{ext,in}} \cdot \eta_{\mathrm{ext,out}})^{-1}$. Assuming that the waveguide facets are identical on both edges of the chip, $\eta_{\mathrm{ext,in}} = \eta_{\mathrm{ext,out}} = \eta_{\mathrm{ext}}$, the external coupling efficiency is $\eta_{\mathrm{ext}} = \sqrt{\eta_{\mathrm{dev}}}$. Supplementary Figure 8b shows the average measured $\eta_{\,\mathrm{ext}}$ for 3 different waveguides as a function of wavelength (the red curve and grey area correspond to the mean and standard deviation over the three measurements, respectively). Averaging this curve across the 1100 nm to 1300 nm wavelength range produces $\eta_{\,\mathrm{ext}} = 0.23 \pm 0.03$ (the uncertainty is obtained by propagating the standard deviations from the three devices). The theoretical mode-mismatch coupling efficiency is calculated with the overlap integral

$$\eta_{\mathrm{facet}} = \frac{\mathrm{Re}\left\{\iint_S (\mathbf{e}_f \times \mathbf{h}^*) \cdot \hat{z}\, dS \iint_S (\mathbf{e} \times \mathbf{h}_f^*) \cdot \hat{z}\, dS\right\}}{\mathrm{Re}\left\{\iint_S (\mathbf{e}_f \times \mathbf{h}_f^*) \cdot \hat{z}\, dS\right\} \mathrm{Re}\left\{\iint_S (\mathbf{e} \times \mathbf{h}^*) \cdot \hat{z}\, dS\right\}} \tag{3}$$

taken over the cross-sectional area S of the input/output Si_3N_4 waveguide. Here, $\mathbf{e}$ and $\mathbf{h}$ are the electric and magnetic field components of the fundamental TE Si_3N_4 input/output waveguide mode (right panel on Fig. 2a), and $\mathbf{e}_f$ and $\mathbf{h}_f$ are the field components of a focused Gaussian beam with a spot size of 2.5 μm. The Gaussian beam spot size is consistent with specifications from the lensed fiber manufacturer. With eq.(3), we obtain $\eta_{\mathrm{facet}} \approx 26$ % for a 580 nm thick $\times$ 800 nm wide Si_3N_4 waveguide, at a wavelength of 1110 nm.

Second-order correlation measurements and fits A Hanbury-Brown and Twiss (HBT) setup was used to obtain the second-order correlation function $g^{(2)}(\tau)$ of QD emission upon continuous-wave pumping. In our experiments, histograms of delays between detection events in the two single-photon detectors were measured. We related these histograms to $g^{(2)}(\tau)$ as explained be-

low. We first calculated delay probability distributions $C(\tau)$ by normalizing the delay histograms. Sufficiently far away from zero time delay, $C(\tau) \approx A \exp(-A\tau)$. We took the 1000 longest-delay bins of our histograms and perform a log-log linear fit to obtain A. The histograms were then normalized by A. For $\tau \approx 0$, $g^{(2)}(\tau) \approx C(\tau)$ (see ref. 42). The $g^{(2)}(\tau)$ data was modeled with the double-exponential function

$$g^{(2)}(\tau) = 1 + A_1 \exp(\lambda_1 \cdot \tau) + A_2 \exp(\lambda_2 \cdot \tau), \tag{4}$$

with $A_1 + A_2 = -1$. This functional form is expected from a two-level system coupled to a single dark state[39], and describes both antibunching at $\tau = 0$, bunching at some later time delay, and a return to the Poissonian level at $\tau \to \infty$. To take into account the $\sigma \approx 129$ ps time-response of detection system (see below for details), we convolved the $g^{(2)}(\tau)$ above with a Normal distribution function $N(\tau, \sigma)$:

$$g_C^{(2)}(\tau) = g^{(2)}(\tau) * N(\tau, \sigma) = 1 + A_1 E_1(\tau) + A_2 E_2(\tau), \tag{5}$$

where

$$E_n(\tau) = \frac{\lambda_n}{2} \exp\left(\frac{\lambda_n \sigma}{2}\right) \left\{ \operatorname{erf}\left(-\frac{\tau}{\sqrt{2}\sigma} + \frac{\lambda_n \sigma}{\sqrt{2}}\right) \mathrm{e}^{-\lambda_n \tau} + \operatorname{erf}\left(\frac{\tau}{\sqrt{2}\sigma} + \frac{\lambda_n \sigma}{\sqrt{2}}\right) \mathrm{e}^{\lambda_n \tau} \right\} \tag{6}$$

and $n = 1, 2$. Finally, to account for a Poissonian background, we used[42]

$$g_{C,B}^{(2)}(\tau) = 1 + \frac{1}{(1+b)^2} \left[g_C^{(2)}(\tau) \right]. \tag{7}$$

The fits shown in the main text were done using $g_{C,B}^{(2)}(\tau)$ above, through a nonlinear least-squares procedure. For the QD in a waveguide of Figs. 5b and 5c, the background b was used as a fit parameter, while for the cavity-coupled QDs of Figs. 6c and 6e , b was fixed at values estimated from fits to emission spectra (see below for spectrum fitting procedures). To plot $g^{(2)}(\tau)$ without the effect of the finite timing resolution, we used $\sigma = 0$ in eq.(6) and used the same fitting parameters. Uncertainties quoted for $g^{(2)}(0)$ are 95 % fit confidence intervals, corresponding to 2 standard deviations.

Photoluminescence spectrum fits The photoluminescence spectra in Figs. 6b and 6f were fitted with a sum of three Lorentzians, representing the cavity and two excitons, X_1 and X_2. A representative fitted spectrum is shown in Fig. 6d, where the individual contributions are also displayed. To produce the left panel on Fig. 6g, the different contributions were multiplied by

a spectrum representing the bandpass grating filter used experimentally, and the X_1 contribution was then normalized to the sum of the integrated intensities of all components before filtering. The wavelength detuning Δ between X_1 and the cavity was determined from these fits. All uncertainties quoted for Δ and the X_1, X_2 and cavity contributions correspond to 95 % fit confidence intervals (two standard deviations).

Photoluminescence decay measurements For excited state lifetime measurements, we employed a 10 GHz lithium niobate electro-optic modulator (EOM) to produce a 80 MHz, $\approx$ 200 ps pulse train from the CW ECDL laser. A fiber-based polarization controller (FPC) was used to control the polarization of the ECDL light going into the EOM, and a DC bias was applied to the EOM to maximize signal extinction. An electrical pulse source was used to produce an 80 MHz train of $\approx$ 200 ps pulses of $<$ 1 V peak amplitude, which was then amplified and used to drive the EOM via its radio frequency (RF) port. A trigger signal from the pulse generator served as the reference channel in our TCSPC system. Supplementary Figure 6a shows a typical temporal profile for the pulses produced by the EOM, detected with an SNSPD. Pulse FWHM of $\approx$ 200 ps and $>$ 20 dB extinction are observed. The pulsed electrical signal produced small satellite peaks that were imprinted in the optical signal, as indicated in Supplementary Figure 6a. These satellite peaks typically appeared a few ns after each proper pulse, and were $\approx$ 20 dB below the latter in intensity. Impulse response functions (IRFs) such as the one in Supplementary Figure 6a were used in decay lifetime fits as explained below, so that the effect of satellite peaks, though minimal, was accounted for. Lastly, to determine the time resolution of our detection system, we launched attenuated few-picosecond pulses from a Ti:Sapphire mode-locked laser at 975 nm into the SNSPDs, to obtain the temporal trace in Supplementary Figure 6b. The peak can be well fitted with a Gaussian with standard deviation σ = 129 ps $\pm$ 0.04 ps (uncertainty is a 95 % least-squares fit confidence interval, corresponding to two standard deviations).

Photoluminescence decay fits Quantum dot emission decay fits were performed using maximum likelihood estimation. We consider a lifetime trace $Y^k = \{Y_i\}_{i=1}^k$ where a known number of photon counts N is distributed over k time bins, such that the bin counts y_i follow a multinomial distribution[43]. The maximum likelihood estimator is

$$g_{MLE}(y^k) = \arg\min_{\boldsymbol{\theta}\in\Theta} \left\{ -\sum_{i=1}^{k} y_i \ln p_i(\boldsymbol{\theta}) \right\}, \tag{8}$$

where $\boldsymbol{\theta}$ is a vector in the multidimensional parameter space Θ. Estimates for the various fit

parameters are obtained by finding $\boldsymbol{\theta}$ that minimizes the expression in the curly brackets, where y_i is the i-th bin count, and $p_i(\boldsymbol{\theta})$ is a probability density function that models the decay, evaluated at the i-th bin. We define $p_i(\tau) = e^{-ir/k}\dfrac{e^{\frac{r}{k}}-1}{1-e^{-r}}$, with $r \triangleq \dfrac{i\cdot\Delta t}{\tau}$. For a monoexponential decay when a portion b of the signal is due to background emission,

$$p_i(\boldsymbol{\theta}) = p_i(\tau, b) = \frac{b}{k} + (1-b)p_i(\tau) \tag{9}$$

For biexponential decay with a background b, let $\tau \triangleq (\tau_1, \tau_2)^T$. Then $p_i(\tau, a, b)$ (where a is the contribution of the first exponential decay) may be expressed as

$$p_i(\boldsymbol{\theta}) = p_i(\tau, b, a) = \frac{b}{k} + (1-b)\left[ap_i(\tau_1) + (1-a)p_i(\tau_2)\right] \tag{10}$$

Variances for the estimated parameters in $\boldsymbol{\theta}$ can be obtained from the diagonal elements of the inverse of the Fisher Information Matrix (see Supplementary Note 8). In the fitting procedure, the trial decay function $p_i(\boldsymbol{\theta})$ is numerically convolved with the experimentally measured, background-subtracted impulse response function (IRF) and used in eq.(8). Because the optical pulses used to obtain the IRF follow a considerably different path length towards the detector than the QD signal, the IRF and QD decay traces are delayed with respect to each other. We manually align the two traces to minimize fit residuals. Uncertainties given in the text correspond to standard deviations for the various parameters, obtained from the diagonal elements of the inverse of the Fisher information matrix computed with the expectation values from the fit (corresponding to the Cramér-Rao lower bound).

Estimate of β Below we estimate the coupling β of the QD exciton at $\lambda \approx 1330.18$ nm of Fig. 5a into the guided TE mode of the GaAs waveguide where it was hosted. Ideally such a measurement would involve saturating the QD under pulsed excitation, where the maximum possible photon flux from the QD is given by the laser repetition rate. Because a pulsed source with sufficient power to saturate the QD was unavailable, our estimate relied on the continuous-wave emission spectrum of Fig. 4a. A three-level system model for the QD was then used to account for blinking. First, we measured the spectrum of a laser signal of known power at 1070 nm with our spectrometer, using the same fiber-coupled input as that for Fig. 5a. The laser was attenuated with a calibrated variable optical attenuator (VOA), and launched into a fiber-based 10:90 power splitter (with a calibrated power-splitting ratio), the 90 % port of which was sent to a photodiode for power monitoring. Integration of the background-subtracted laser spectrum counts divided by the laser power gave a factor of 0.0023 counts per photon at the spectrometer fiber-coupled input (this

includes losses at the fiber connector, spectrometer slit, grating and output slit before the InGaAs detector array). This allowed us to obtain, from the fitted QD spectrum of Fig. 5a, a photon flux $P = 3.0 \times 10^6$ s$^{-1} \pm 0.5 \times 10^6$ s^{-1} (errors come from the 95 % fit confidence intervals) at this fiber input for the 1130.18 nm exciton line (accounting for the wavelength difference). We next expanded the photon flux as $P = X\beta\eta\eta_{\text{ext.}}\eta_{\text{TF}}$, where X is the exciton population probability, η the mode transformer efficiency, $\eta_{\text{ext.}}$ the lensed fiber-to-chip coupling efficiency, and $\eta_{\text{TF}} = 0.91 \pm 0.03$ is the lensed fiber transmission (uncertainty from measurement error, corresponding to one standard deviation). Solving the three-level system rate equations (with one bright and one dark transition) that fit the $g^{(2)}(\tau)$ data in Fig. 4c - assuming the lifetime in Fig. 4d for the bright transition - we obtain $X = 0.15 \pm 0.04$, where the uncertainty is the 95 % fit confidence interval. We note that connecting the dark state to either the ground or bright excited state in our model leads to $X \approx 0.15$. Assuming $\eta = 98$ % (the maximum from simulation) and $\eta_{ext.} = 0.22$, a reasonable value from Supplementary Figure 8b at 1130 nm, we obtain, propagating uncertainties, $\beta = 0.20 \pm 0.07$.

Data Availability All data supporting this study are openly available from the University of Southampton repository at http://doi.org/10.5258/SOTON/D0174.

* Electronic address: marcelo.davanco@nist.gov

† Electronic address: liujin23@mail.sysu.edu.cn

‡ Electronic address: kartik.srinivasan@nist.gov

References

[1] J. L. O'Brien, A. Furusawa, and J. Vučković, "Photonic quantum technologies," Nature Photonics **3**, 687–695 (2009).

[2] P. Kok, W. J. Munro, K. Nemoto, T. C. Ralph, J. P. Dowling, and G. J. Milburn, "Linear optical quantum computing with photonic qubits," Rev. Mod. Phys. **79**, 135–174 (2007).

[3] A. Politi, M. J. Cryan, J. G. Rarity, S. Yu, and J. L. O'Brien, "Silica-on-Silicon Waveguide Quantum Circuits," Science **320**, 646–649 (2008).

[4] S. Tanzilli, A. Martin, F. Kaiser, M. De Micheli, O. Alibart, and D. Ostrowsky, "On the genesis and evolution of Integrated Quantum Optics," Laser & Photonics Reviews **6**, 115–143 (2012).

[5] T. C. Ralph, "Quantum computation: Boson sampling on a chip," Nature Photonics **7**, 514–515 (2013).

[6] J. C. Loredo, M. A. Broome, P. Hilaire, O. Gazzano, I. Sagnes, A. Lemaitre, M. P. Almeida, P. Senellart, and A. G. White, "BosonSampling with single-photon Fock states from a bright solid-state source," Physical Review Letters **118**, 130 503 (2017).

[7] Q. Li, M. Davanço, and K. Srinivasan, "Efficient and low-noise single-photon-level frequency conversion interfaces using silicon nanophotonics," Nature Photonics **10**, 406–414 (2016).

[8] R. Riedinger, S. Hong, R. A. Norte, J. A. Slater, J. Shang, A. G. Krause, V. Anant, M. Aspelmeyer, and S. Gröblacher, "Non-classical correlations between single photons and phonons from a mechanical oscillator," Nature **530**, 313–316 (2016).

[9] D. E. Chang, V. Vuletić, and M. D. Lukin, "Quantum nonlinear optics photon by photon," Nature Photonics **8**, 685–694 (2014).

[10] A. Reiserer and G. Rempe, "Cavity-based quantum networks with single atoms and optical photons," Rev. Mod. Phys. **87**, 1379–1418 (2015).

[11] N. Somaschi, V. Giesz, L. De Santis, J. C. Loredo, M. P. Almeida, G. Hornecker, S. L. Portalupi, T. Grange, C. Antón, J. Demory, C. Gmez, I. Sagnes, N. D. Lanzillotti-Kimura, A. Lemaitre, A. Auffeves, A. G. White, L. Lanco, and P. Senellart, "Near-optimal single-photon sources in the solid state," Nature Photonics **10**, 340–345 (2016).

[12] X. Ding, Y. He, Z.-C. Duan, N. Gregersen, M.-C. Chen, S. Unsleber, S. Maier, C. Schneider, M. Kamp, S. Höfling, C.-Y. Lu, and J.-W. Pan, "On-Demand Single Photons with High Extraction Efficiency and Near-Unity Indistinguishability from a Resonantly Driven

Quantum Dot in a Micropillar," Physical Review Letters **116**, 020 401 (2016).

[13] R. J. Warburton, "Single spins in self-assembled quantum dots," Nature Materials **12**, 483–493 (2013).

[14] K. Srinivasan and O. Painter, "Linear and nonlinear optical spectroscopy of a strongly coupled microdisk-quantum dot system," Nature **450**, 862–865 (2007).

[15] S. Sun, H. Kim, G. S. Solomon, and E. Waks, "A quantum phase switch between a single solid-state spin and a photon," Nature Nanotechnology **11**, 539–544 (2016).

[16] I. Fushman, D. Englund, A. Faraon, N. Stoltz, P. Petroff, and J. Vučković, "Controlled Phase Shifts with a Single Quantum Dot," Science **320**, 769–772 (2008).

[17] C. Xiong, X. Zhang, A. Mahendra, J. He, D.-Y. Choi, C. J. Chae, D. Marpaung, A. Leinse, R. G. Heideman, M. Hoekman, C. G. H. Roeloffzen, R. M. Oldenbeuving, P. W. L. van Dijk, C. Taddei, P. H. W. Leong, and B. J. Eggleton, "Compact and reconfigurable silicon nitride time-bin entanglement circuit," Optica **2**, 724–727 (2015).

[18] T. P. Purdy, K. E. Grutter, K. Srinivasan, and J. M. Taylor, "Quantum correlations from a room-temperature optomechanical cavity," Science **356**, 1265–1268 (2017).

[19] J. E. Bowers, T. Komljenovic, M. Davenport, J. Hulme, A. Y. Liu, C. T. Santis, A. Spott, S. Srinivasan, E. J. Stanton, and C. Zhang, "Recent advances in silicon photonic integrated circuits,", Proc. SPIE **9774**, 977402 (2016).

[20] I. Aharonovich, D. Englund, and M. Toth, "Solid-state single-photon emitters," Nature Photonics **10**, 631–641 (2016).

[21] J. Bleuse, J. Claudon, M. Creasey, N. S. Malik, J.-M. Gérard, I. Maksymov, J.-P. Hugonin, and P. Lalanne, "Inhibition, Enhancement, and Control of Spontaneous Emission in Photonic Nanowires," Phys. Rev. Lett. **106**, 103 601 (2011).

[22] J. Claudon, J. Bleuse, N. S. Malik, M. Bazin, P. Jaffrennou, N. Gregersen, C. Sauvan, P. Lalanne, and J. Gérard, "A highly efficient single-photon source based on a quantum dot in a photonic nanowire," Nature Photonics **4**, 174–177 (2010).

[23] M. Davanço and K. Srinivasan, "Fiber-coupled semiconductor waveguides as an efficient optical interface to a single quantum dipole," Opt. Lett. **34**, 2542–2544 (2009).

[24] M. Davanço, M. T. Rakher, W. Wegscheider, D. Schuh, A. Badolato, and K. Srinivasan, "Efficient quantum dot single photon extraction into an optical fiber using a nanophotonic directional coupler," Applied Physics Letters **99**, 121 101 (2011).

[25] I. E. Zadeh, A. W. Elshaari, K. D. Jöns, A. Fognini, D. Dalacu, P. J. Poole, M. E.

Reimer, and V. Zwiller, "Deterministic Integration of Single Photon Sources in Silicon Based Photonic Circuits," Nano Lett. **16**, 2289–2294 (2016).

[26] A. W. Elshaari, I. E. Zadeh, A. Fognini, M. E. Reimer, D. Dalacu, P. J. Poole, V. Zwiller, and K. D. Jöns, "On-Chip Single-Photon Sifter." Pre-print at https://arxiv.org/abs/1611.03245v3 (2016).

[27] V. S. C. Manga Rao and S. Hughes, "Single quantum-dot Purcell factor and β factor in a photonic crystal waveguide," Physical Review B **75**, 205 437 (2007).

[28] T. Lund-Hansen, S. Stobbe, B. Julsgaard, H. Thyrrestrup, T. Sünner, M. Kamp, A. Forchel, and P. Lodahl, "Experimental Realization of Highly Efficient Broadband Coupling of Single Quantum Dots to a Photonic Crystal Waveguide," Physical Review Letters **101**, 113 903 (2008).

[29] X. Sun, H.-C. Liu, and A. Yariv, "Adiabaticity criterion and the shortest adiabatic mode transformer in a coupled-waveguide system," Optics Letters **34**, 280–282 (2009).

[30] R. J. Coles, D. M. Price, J. E. Dixon, B. Royall, E. Clarke, P. Kok, M. S. Skolnick, A. M. Fox, and M. N. Makhonin, "Chirality of nanophotonic waveguide with embedded quantum emitter for unidirectional spin transfer," Nature Communications **7**, 11 183 (2016).

[31] I. Söllner, S. Mahmoodian, S. L. Hansen, L. Midolo, A. Javadi, G. Kiransk, T. Pregnolato, H. El-Ella, E. H. Lee, J. D. Song, S. Stobbe, and P. Lodahl, "Deterministic photonemitter coupling in chiral photonic circuits," Nature Nanotechnology **10**, 775–778 (2015).

[32] A. Young, A. Thijssen, D. Beggs, P. Androvitsaneas, L. Kuipers, J. Rarity, S. Hughes, and R. Oulton, "Polarization Engineering in Photonic Crystal Waveguides for Spin-Photon Entanglers," Physical Review Letters **115**, 153901 (2015).

[33] A. Stintz, G. T. Liu, H. Li, L. F. Lester, and K. J. Malloy, "Low-threshold current density 1.3-μm InAs quantum-dot lasers with the dots-in-a-well (DWELL) structure," IEEE Photonics Technology Letters **12**, 591–593 (2000).

[34] L. Sapienza, M. Davanço, A. Badolato, and K. Srinivasan, "Nanoscale optical positioning of single quantum dots for bright and pure single-photon emission," Nature Communications **6**, 7833 (2015).

[35] J. Liu, M. I. Davanco, L. Sapienza, K. Konthasinghe, J. V. D. M. Cardoso, J. D. Song, A. Badolato, and K. Srinivasan, "Cryogenic photoluminescence imaging system for nanoscale positioning of single quantum emitters," Review of Scientific Instruments

88, 023 116 (2017).

[36] A. Dousse, L. Lanco, J. Suffczyński, E. Semenova, A. Miard, A. Lemaître, I. Sagnes, C. Roblin, J. Bloch, and P. Senellart, "Controlled Light-Matter Coupling for a Single Quantum Dot Embedded in a Pillar Microcavity Using Far-Field Optical Lithography," Physical Review Letters **101**, 267 404 (2008).

[37] F. Marsili, V. B. Verma, J. A. Stern, S. Harrington, A. E. Lita, T. Gerrits, I. Vayshenker, B. Baek, M. D. Shaw, R. P. Mirin, and S. W. Nam, "Detecting single infrared photons with 93% system efficiency," Nature Photonics **7**, 210–214 (2013).

[38] C. Santori, D. Fattal, J. Vučković, G. S. Solomon, E. Waks, and Y. Yamamoto, "Submicrosecond correlations in photoluminescence from InAs quantum dots," Physical Review B **69**, 205 324 (2004).

[39] M. Davanço, C. S. Hellberg, S. Ates, A. Badolato, and K. Srinivasan, "Multiple time scale blinking in InAs quantum dot single-photon sources," Physical Review B **89**, 161 303 (2014).

[40] K. Srinivasan and O. Painter, "Optical fiber taper coupling and high-resolution wavelength tuning of microdisk resonators at cryogenic temperatures," Applied Physics Letters **90**, 031 114 (2007).

[41] W. Pernice, C. Schuck, O. Minaeva, M. Li, G. Goltsman, A. Sergienko, and H. Tang, "High-speed and high-efficiency travelling wave single-photon detectors embedded in nanophotonic circuits," Nature Communications **3**, 1325 (2012).

[42] R. Verberk and M. Orrit, "Photon statistics in the fluorescence of single molecules and nanocrystals: Correlation functions versus distributions of on- and off-times," The Journal of Chemical Physics **119**, 2214–2222 (2003).

[43] M. Köllner and J. Wolfrum, "How many photons are necessary for fluorescence-lifetime measurements?" Chemical Physics Letters **200**, 199–204 (1992).

Acknowledgements We thank Daron Westly and Rob Ilic from the NIST CNST for invaluable aid with fabrication, and Raphael Daveau from the Niels Bohr Institute, University of Copenhagen, Denmark, for aid with the optical setup. J.L. acknowledges the Ministry of Science and Technology of China (grant no. 2016YFA0301300), the National Natural Science Foundation of China(grant no. 11304102), and support under the Cooperative Research Agreement between the University of Maryland and NIST-CNST, Award 70NANB10H193. L.S. acknowledges financial support from

EPSRC, grant EP/P001343/1. J.V.D.M.C. acknowledges funding from the Brazilian Ministry of Education through the Brazilian Scientific Mobility Program CAPES-grant 88888.037310/2013-00.

Author Contributions M.D. developed computational electromagnetics models and designed the devices, developed the fabrication process, designed and performed the experiments, analyzed the data and wrote the manuscript. J.L. produced wafer-bonded samples, performed experiments and wrote the manuscript. L.S. performed experiments and wrote the manuscript. C.-Z.Z. and L.L. designed devices and produced wafer-bonded samples. J.V.D.M.C. wrote the lifetime fitting scripts. V.V., R.M. and S.W.N. provided the nanowire superconducting single-photon detectors. K.S. supervised the project and wrote the manuscript.

Competing financial interests The authors declare no competing financial interests.

Supplementary Note 1 - Quantum photonic integrated circuits with quantum dots

The considerable potential of InAs/GaAs quantum dots (QDs), both for triggered single-photon generation and as quantum logic elements, has spurred the development of a number of platforms that seek to incorporate these QDs within photonic circuits. A direct method is to develop both active and passive components within the same material system. Along these lines, monolithic GaAs-based quantum photonic circuits with on-chip quantum dot-based single-photon sources have been demonstrated by a number of research groups [1]. Two general approaches have been adopted. In the first, passive circuits are composed of low-index-contrast GaAs/AlGaAs ridge waveguides produced on top of a GaAs/AlGaAs substrate [2, 3]. Such waveguide geometries can be produced with relatively straightforward fabrication processes, relying solely on epitaxial growth for vertical optical confinement and a single etching step for lateral confinement. Due to the small vertical refractive index contrast that is achievable through growth, waveguide cross-section dimensions are typically of the order of microns. While lower refractive indices are generally desirable for minimizing scattering losses in propagation, large mode field diameters (and large mode volumes in the case of cavities) translate into less compact devices, less effective light-matter interactions, and less effective geometrical control of waveguide dispersion (relevant for on-chip nonlinear optics). In particular, weak vertical confinement means more effective dipolar coupling to substrate radiative modes, translating into a reduced β-factor for radiating dipoles (see main text). Distributed-feedback reflector-based geometries such as in ref. 2 can ameliorate this, however the achievable mode-field diameters are also limited by the relatively small index contrast between GaAs and AlGaAs. All of these issues are to great extent circumvented in the second approach, in which circuits composed of suspended GaAs waveguides surrounded by air or vacuum, either of the channel [4] or photonic crystal [5] types (or both), are implemented. In this case, the strong index contrast allows strong transverse field confinement in waveguides of cross-sectional dimensions of the order of hundreds of nanometers. Small modal areas and cavity mode volumes can be achieved, meaning stronger light-matter interactions and higher β-factors for radiating dipoles [6], together with strong geometry-based control of waveguide dispersion. An important limitation of such an approach, however, is the losses due to scattering at the etched sidewalls, which can be considerably higher due to the strong index contrast between the semiconductor and the air. A second issue is that the fragility of suspended GaAs structures imposes limits on the dimensions of free-standing circuits, requiring support structures such as tethers or transitions to non-suspended waveguides, which may induce significant scattering losses [5]. Fabrication, device handling, and further integration with other types of on-chip elements are also more cumbersome in this case. An additional challenge common to both approaches is that passive circuits are produced in the same material layer that contains the QDs. Because there is no strict separation between active and passive portions of the photonic circuit, the population of QDs inside the passive section can contribute to excess optical absorption.

As discussed in the main text, our heterogeneous integration platform offers essentially all the advantages of the two approaches described above, while addressing many of the aforementioned challenges. The large refractive index contrast between GaAs and Si_3N_4 allows for strong modal confinement within the GaAs layer so that large β factors can be achieved in the active quantum dot region. This large refractive index contrast is, in addition, achieved without requiring devices to be undercut, improving the mechanical and thermal stability of the system, particularly as the number of integrated elements increases. Furthermore, complete removal of the GaAs material outside in the passive regions avoids excess optical absorption due to the background QD ensemble. Within the passive sections, the large refractive index contrast between Si_3N_4 and SiO_2 enables the dispersion engineering and large effective nonlinearity needed for nonlinear optics applications, such as frequency downconversion of the QD emission to the 1550 nm telecom band [7]. Such nonlinear optics applications can in principle be implemented in suspended GaAs photonic circuits, though the much wider bandgap of Si_3N_4 and SiO_2 in comparison to GaAs-based materials ensures that two-photon absorption, an important factor in nonlinear nanophotonic devices, is negligible over a wide range of wavelengths. Coupling off-chip to optical fibers can also be optimized, as our platform is compatible with end-fire approaches that utilize inverse tapers and symmetric low-index claddings [8, 9]. In particular, devices can be designed to admit a full SiO_2 cladding rather than the current top air cladding, with additional processing likely consisting of a single additional PECVD deposition step.

To make the distinction between the homogeneous GaAs-based photonic circuit platforms described above and our hybrid geometry more evident, in Supplementary Figures 1a-e we plot field profiles for representative waveguides of all types mentioned above. It is visually apparent that the modal areas achieved in our platform (Supplementary Figure 1d) are comparable to those obtained with suspended waveguides (Supplementary Figure 1a), of either channel [4] or photonic crystal [5] kind. The modal areas of our GaAs-on-Si_3N_4/SiO_2 waveguides are considerably smaller than the modal areas of all of the GaAs-based waveguides on GaAs/AlGaAs substrate [2, 3], shown in Supplementary Figures. 1b and c. More quantitatively, we display, for the plotted fundamental modes in each geometry, the effective area $A_{\text{eff}} = \int \epsilon_r |\mathbf{E}|^2 dS / \max\{|\mathbf{E}|^2\}$, where $\mathbf{E}$ is the electric field, ϵ_r is the relative permittivity and the integral is taken over the waveguide cross-section. This quantity is inversely proportional to the maximum interaction strength between the guided mode and a single quantum emitter inside the waveguide [11], and essentially serves as a measure

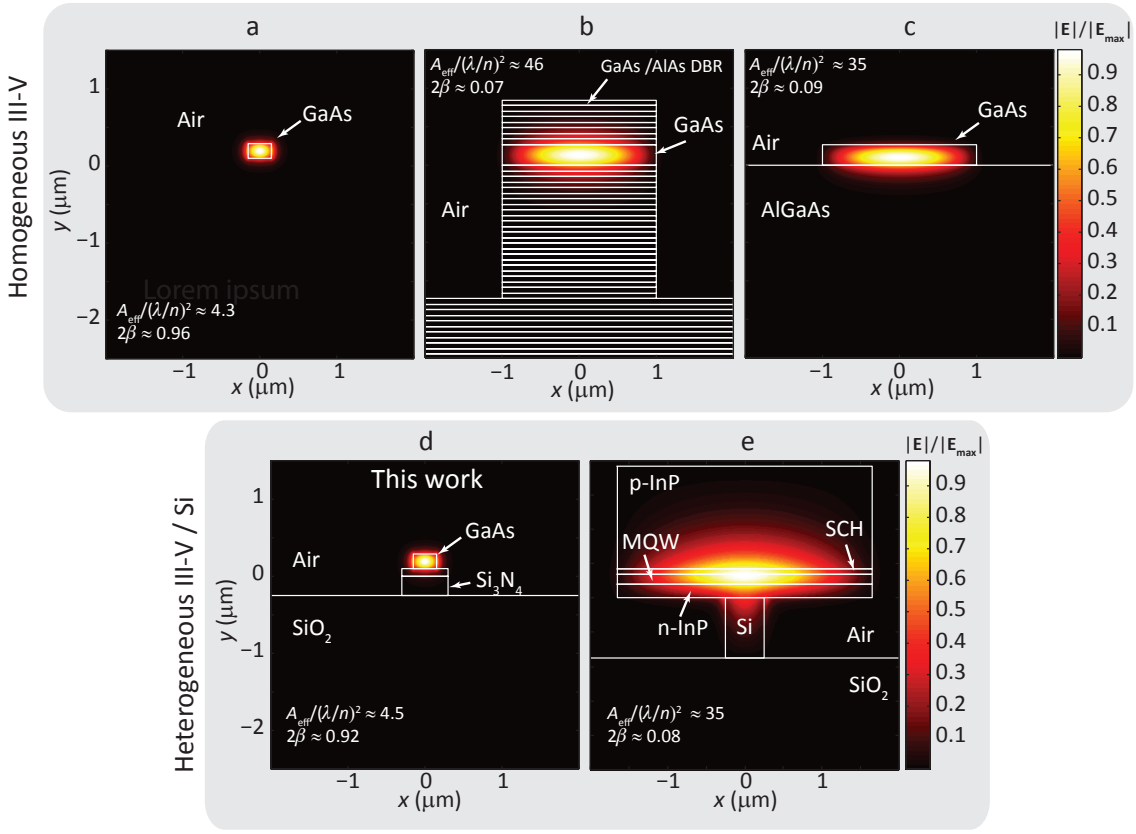

Supplementary Figure 1: **Comparison of waveguide geometries for single quantum dots**. Electric field profiles for the fundamental modes of **a**, suspended GaAs [4]; **b**, distributed feedback reflector (DBR) ridge [2]; **c**, GaAs/AlGaAs ridge [3]; **d**, GaAs / Si_3N_4 hybrid waveguides; and **e**, InP/InGaAsP/Si hybrid waveguides [10], with corresponding effective areas (normalized by $(\lambda/n)^2$, the corresponding squared wavelength in the semiconductor) and β-factors. Notes: 1) Photonic crystal waveguides [5], at frequencies away from slow-light band-edges, have similar cross-sectional modal profiles, effective areas and β-factors as the suspended channel guide in **a**. 2) The GaAs/AlGaAs ridge waveguide in **c** was chosen to have the same width as the DBR guide in **c**, for a fairer comparison; the original guide from ref. 3 had a width of 20 μm, which leads to a significantly larger effective area and lower β. 3) The InP/InGaAsP/Si hybrid geometry shown in **e** is typical for Si photonic laser geometries at telecom ($\approx$ 1550 nm) wavelengths. MQW: multi-quantum well. SCH: separate confinement heterostructure.

of the field concentration at the emitter location, assumed to be at the field maximum (an alternative definition that includes ϵ_r^2 in the denominator, analogous to that used for the effective volume in cavities, would yield effective areas smaller by a factor of $n^2 \approx (3.5)^2$, with n the refractive index of the III-V medium). We also provide the β-factor for each geometry. It is clear that modal areas in the suspended and hybrid geometries are roughly an order of magnitude smaller than in the GaAs geometries. In addition, $\beta > 90$ % is only achieved in suspended or hybrid structures. Both features are achieved through the high refractive index step between either air or Si_3N_4, which provides a sufficiently strong vertical confinement.

Lastly, while heterogeneous integration of active III-V layers and passive silicon-on-insulator waveguides has become an important technology in classical photonics [10, 12, 13], as noted in the main text, the specific geometries typically used are not necessarily suitable for quantum photonics. To illustrate this point, we make a comparison with geometries typical of Si photonic lasers [10] as shown in Supplementary Figure 1e. In this hybrid geometry, the Si ridge provides low-loss waveguiding, whereas the III-V layer provides optical gain through an InGaAsP multi-quantum well (MQW) heterostructure which is electrically pumped through the top and bottom p- and n-type InP layers. An InGaAsP separate confinement heterostructure (SCH) above the MQW acts as guiding core, providing a weak vertical optical confinement that results in the mode shown in the Figure, extending deeply into the p-InP layer. The p-InP layer is necessarily made thick in order to minimize propagation losses due to absorption at the electrical contact layers which top the III-V stack (not shown in the figure, generally consisting of a highly p-doped InP contact and a metal layer [12]). The effective area for such a mode is of the order of $35(\lambda/n)^2$, considerably larger than obtained with our strongly confining hybrid geometry, indicating a considerably smaller light-matter interaction strength. The

$2\beta \approx 0.08$ is also considerably lower. Both of these factor indicate that this geometry is far from optimal for probing single embedded emitters. It is worth pointing out that such large effective areas and low β-factors are comparable to those achieved in purely GaAs-based geometries with weak modal confinement discussed above.

While all of the fabrication steps that we have demonstrated in this work are scalable, the random nature of the in-plane spatial locations of self-assembled InAs/GaAs QDs is a limitation on the overall yield and ability to, for example, integrate multiple QD sites together within a passive Si_3N_4 circuit. Going forward, developments in site-controlled QD growth [14–16] will help to address this issue, and in general will be compatible with our fabrication approach. In the near-term, we can envision pre-characterization of QDs after creating the bonded wafer stack, such that GaAs devices are only created in regions for which desirable single QD behavior has been confirmed. In particular, photoluminescence imaging [17] has been confirmed as a technique for locating the position of single InAs/GaAs QDs with respect to alignment features, and recent implementations [18] have demonstrated the location of single QDs within ≈ 5000 μm^2 spatial regions with sub-10 nm positioning uncertainty, with typical image acquisition times of 1 s. We anticipate that such an approach can enable a higher throughput than pick-and-place techniques [19–22], which also require pre-screening of the quantum emitters along with the additional assembly steps.

We have summarized all of the differences between our platform and others in Supplementary Table 1.

	Low-loss propagation	Strong mode confinement and light-matter interaction	Mechanical Stability	Scalable top-down fabrication	Wideband optical nonlinearity
Suspended GaAs		×		×	see caption
DBR ridge			×	×	see caption
GaAs/AlGaAs ridge			×	×	see caption
Ref. 19	×		×		×
This work	×	×	×	×	×

Supplementary Table 1: **Comparison of existing platforms for integrated quantum photonics**. While III-V materials can have large $\chi^{(2)}$ or $\chi^{(3)}$, two-photon absorption (TPA) might limit the useful operating wavelength range of nonlinear optical phenomena. For GaAs, for example, pumps at wavelengths above 1700 nm are generally required to avoid TPA.

Supplementary Note 2 - Fabrication Details

To produce the starting wafer stack shown in Fig. 3a of the main text, we utilized the low-temperature plasma-activated direct wafer bonding procedure of ref. 12. The layer stack for the two wafers that are bonded in this procedure, one silicon-based and one GaAs-based, are given in Supplementary Tables 2 and 3 respectively. The Si_3N_4 layer of the silicon-based stack in Supplementary Table 2 was grown with low-pressure chemical vapor deposition, and the epilayer stack of Supplementary Table 3 was grown via molecular beam epitaxy.

Layer	Material	Thickness (nm)
Waveguide	Si_3N_4	550
Bottom cladding	Thermal SiO_2	3000
Substrate	Si	-

Supplementary Table 2: **Si_3N_4 wafer stack**

Layer	Material	Thickness (nm)
Surface cap	GaAs	10
Waveguide top	$Al_{0.30}Ga_{0.70}As$	40
Waveguide top	GaAs	74
Quantum well	$In_{0.15}Ga_{0.85}As$	6
Quantum dot	InAs	2.4 monolayer
Barrier	$In_{0.15}Ga_{0.85}As$	1
Waveguide bottom	GaAs	74
Sacrificial layer	$Al_{0.30}Ga_{0.70}As$	50
Sacrificial layer	$Al_{0.70}Ga_{0.30}As$	1500
Substrate	GaAs	-

Supplementary Table 3: **GaAs Epilayer Stack**

A $\approx$ 30 nm layer of SiN was deposited on top of cleaved ($\approx$ 5 mm^2) pieces of the III-V epiwafer with plasma-enhanced chemical vapor deposition (PECVD). Contact lithography followed by reactive ion etching in a $CHF_3/O_2/Ar$ plasma was used to produce $\approx 10\,\mu$m wide, $\approx$ 1 cm long, $\approx$ 30 nm deep channels on the Si_3N_4 wafer surface, prior to bonding. This was done to prevent the formation of trapped H_2 bubbles at the bonding interface during the annealing process [12]. The Si_3N_4 wafer was then cleaved into small ($\approx$ 2 cm^2) pieces.

For wafer bonding, the surfaces of the GaAs and Si_3N_4 wafer pieces were cleaned in acetone, then activated in an O_2 plasma for 1 minute, at a pressure of 26.7 Pa (200 mTorr), flow of 1.5×10^{-5} O_2 mol/s (20 sccm) and 200 W radio-frequency power. Pairs of wafers were then placed in contact and pre-bonded under light manual contact. The pre-bonded samples were next annealed at 300 °C for 1 hour in a nitrogen-purged environment to produce a permanent bond. The warm-up and cool-down rates were set to 5 °C/min. At this point, samples consisted of small, rectangular-shaped GaAs wafer pieces permanently bonded onto the surface of larger Si_3N_4 wafers.

We next carefully covered the exposed Si_3N_4 areas on the wafers with Apiezon W wax [23] that had been previously dissolved in trichloethylene (TCE). The dissolved wax wetted the Si_3N_4 surfaces and the sidewalls of the bonded GaAs pieces, however not the exposed back surfaces of the GaAs wafer. We placed the samples on a hotplate at 80 °C for 30 minutes to evaporate the TCE, solidifying the wax. The samples were next immersed in a 3:7 H_3PO_4:H_2O_2 solution for approximately 5 hours, to remove most of the GaAs substrate. They were then transferred to a 4:1 citric acid (50 % mass fraction):H_2O_2 solution, which etched GaAs with a very high selectivity with respect to the AlGaAs sacrificial layers. The samples were left in for approximately 5 hours, until the exposed GaAs wafer surface looked uniform and unchanged. At this point, the GaAs substrate had been completely removed. Next, the samples were dipped in 49 % HF for 30 seconds to remove the AlGaAs sacrifial layers. Finally, the wax was removed with TCE.

Following the wafer bonding step, fabrication proceeded as described in the main text. Further details are provided here. An array of Au alignment marks was first produced on top of the GaAs layer via electron-beam lithography followed by metal-lift-off. A bilayer polymethylmethacrylate/copolymer resist process was used. An electron-beam evaporator was used to deposit a 10 nm Cr adhesion layer, and a 50 nm Au layer. Lift-off was carried out in an acetone bath. Electron-beam lithography with ZEP 520A [23] resist followed by inductively-coupled plasma etching using a Cl_2:Ar chemistry were next used to define GaAs devices aligned to the Au mark array. Because ZEP520A is a positive-tone resist, devices were defined by etching the GaAs only in micron-size areas that surrounded the devices. To remove the remaining GaAs from the rest of the wafer surface, we used a wet-etch approach. First,

e-beam lithography with ma-N 2045negative tone resist [23] was performed to define protection patterns that covered only the device areas and a selected number of Au alignment marks (a protection patch is highlighted in the optical micrograph in Fig. 3b of the main text, covering the GaAs microring resonator and bus waveguide). The samples were then immersed in TFA gold etchant for ≈ 1 min, then in 1020 Cr etch solution for ≈ 1 min. This removed exposed Cr/Au alignment marks, as well as the exposed GaAs layer. The wet etch procedure could be repeated several times without affecting the resist protection layer. Acetone was afterwards used to remove the ma-N resist.

After cleanup of the etched sample surface, a second electron-beam lithography exposure was performed, referenced to the original Au mark array, to define Si_3N_4 waveguide patterns aligned to the previously etched GaAs devices. We emphasize that the alignment marks used were from the original mark array, and were protected during the GaAs wet etch step. Reactive ion etching (RIE) in a CHF_3/CF_4 plasma was used to produce the Si_3N_4 waveguides. The chip was finally cleaved perpendicular to the Si_3N_4 waveguides > 1 mm away from the GaAs devices, to allow access with optical fibers in the endfire configuration.

Supplementary Note 3 - Optimized dipole coupling into the hybrid waveguide

Here we present simulation results for the fundamental TE GaAs mode β-factor of two optimized emission capture structures. In both cases, the active waveguide section is a as shown in Supplementary Figure 2a. The GaAs waveguide has a thickness of 190 nm, and the Si_3N_4 waveguide width is 600 nm. A 100 nm layer of SiO_2 separates the two waveguides. Such a layer can be produced with PECVD, same as the nitride layer grown on our GaAs wafer prior to bonding, without adversely affecting the bond quality. For the first optimized geometry, see Supplementary Figure 2b, the Si_3N_4 thickness is 550 nm, similar to the Si_3N_4 waveguides in our sample. In Supplementary Figure 2b, the Si_3N_4 thickness is 250 nm. In both cases, $\beta > 0.46$ for modes propagating in either $+z$ or $-z$ directions ($2\beta > 0.92$ altogether), for a wavelength range of tens of nanometers around 1100 nm, for GaAs waveguide widths close to 300 nm.

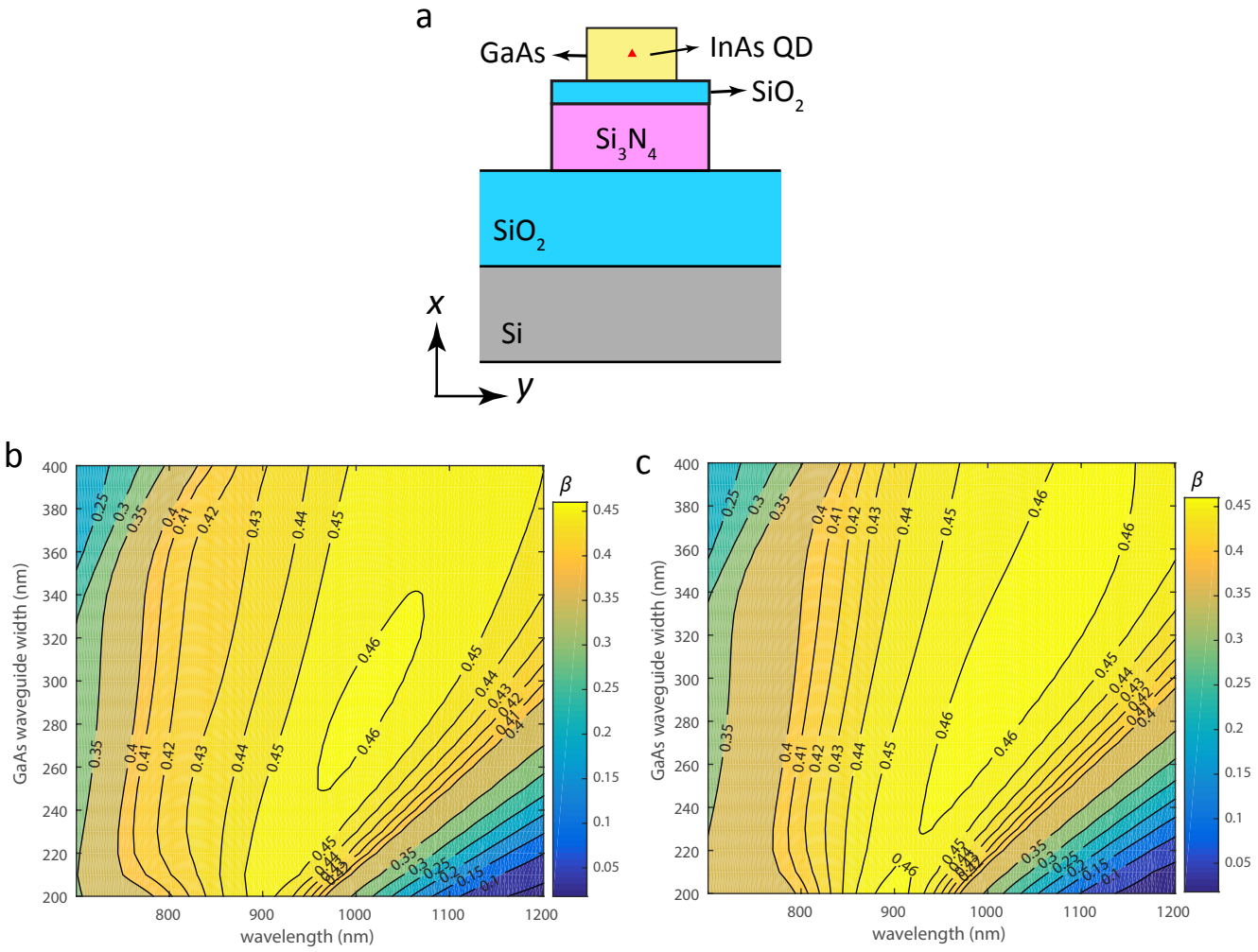

Supplementary Figure 2: **β-factors in optimized structures**. **a** Emission capture structure cross-section. **b**, β factors as a function of wavelength and GaAs waveguide width for the fundamental TE GaAs mode, for a GaAs waveguide with thickness of 190 nm, Si_3N_4 waveguide has a width of 600 nm and thickness of 550 nm. A 100 nm thick layer of SiO_2 separates the Si_3N_4 and GaAs waveguides. The Si_3N_4 dimensions here are relevant for optical nonlinearities, as discussed in the main text. **c**, same as **a** for a 250 nm Si_3N_4 thickness, relevant for linear optics applications.

Supplementary Note 4 - Small mode-volume resonances for strong-coupling regime cavity QED

Here we present simulation results for waveguide-coupled microdisks within our platform, with which the strong-coupling cavity QED regime might be achieved. We first point out that in ref. 24, strong-coupling was achieved in a 2.5 um diameter air-clad microdisk resonator that supported a whispering-gallery mode at $\lambda \approx 1300$ nm, with quality factor $Q \approx 1 \times 10^5$, and standing-wave mode volume $V_{\text{eff}} \approx 3 \times (\lambda/n)^3$. Within our platform, a similar quantum dot-containing GaAs microdisk resonator geometry can be implemented as shown in the schematic of Supplementary Figure 3a. The GaAs microdisk can can be accessed through a GaAs bus waveguide, which is in turn efficiently coupled to the Si_3N_4 waveguide via the mode transformer geometries. The GaAs microdisk contains a single InAs quantum dot, which we next theoretically show can be strongly coupled to a whispering gallery mode of the GaAs/Si_3N_4 microdisk resonator, shown in Supplementary Figure 3b. As in ref. 24, we estimate the coherent coupling rate g_0 between the quantum dot and a standing-wave type whispering-gallery mode in the strong-coupling regime to be

$$g_0 = \frac{1}{2\tau_{\text{sp}}}\sqrt{\frac{3c\tau_{\text{sp}}}{2\pi\lambda V_{\text{eff}}/(\lambda/n)^3}}, \tag{1}$$

where τ_{sp} is the natural quantum dot spontaneous emission lifetime, n is the GaAs refractive index, λ is the wavelength of the whispering-gallery mode. Supplementary Figure 3b shows a cross-sectional field amplitude map of the azimuthal $m = 18$ whispering-gallery mode for a hybrid GaAs microdisk of height 200 nm and diameter 2 μm within our platform, calculated with the finite-element method. The hybrid resonator consists of a GaAs microdisk that sits on top of a 250 nm thick Si_3N_4 cylinder of radius 1.2 μm, over a SiO_2 substrate. The calculated radiation-limited quality factor here is $Q_{\text{rad}} \approx 10^9$, and the standing-wave mode volume is $V_{\text{eff}} \approx 6(\lambda/n)^3$. Using this value in Eq. (1), together with the typical parameters $\tau_{\text{sp}} = 1$ ns, $n = 3.4$ and $\lambda = 937$ nm for InAs quantum dots, we obtain $g_0/2\pi \approx 13$ GHz. With this, the strong coupling regime can be within reach for realistic quantum dot linewidths (< 1 GHz) and coupled-cavity quality factors, $Q \approx 1 \times 10^4$ (corresponding to a cavity decay rate $\kappa \approx 6$ GHz).

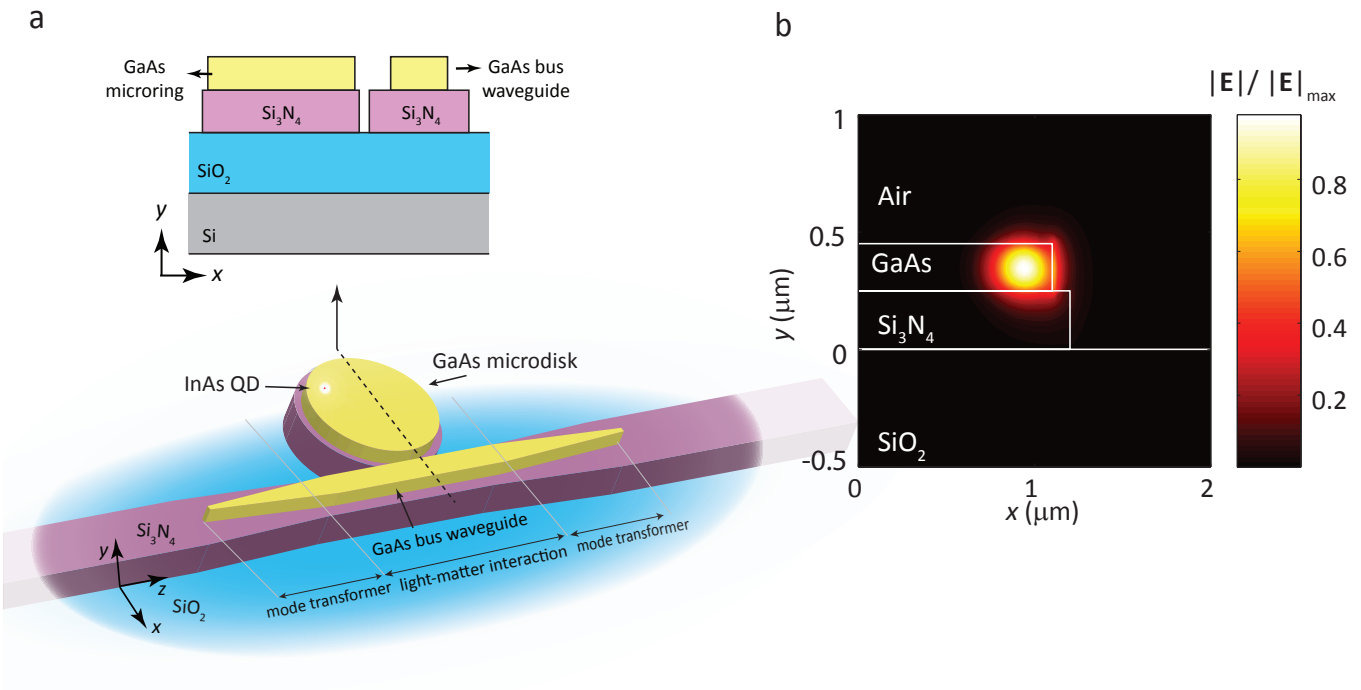

Supplementary Figure 3: **Hybrid microdisk whispering-gallery modes for strong coupling**. **a**, Schematic of waveguide-coupled hybrid microdisk resonator within out platform. The top image shows a cross-section of the geometry, corresponding to the dashed line in the 3D schematic. **b**, Cross-sectional electric field amplitude profile for the $m = 18$ azimuthal whispering-gallery hybrid microdisk mode, which has a standing wave mode volume of $6(\lambda/n)^3$ and a predicted vacuum coupling strength of 13 GHz to a single, optimally aligned quantum dot.

We note that although a microdisk geometry was chosen in this example, we expect very similar results for similar-sized microrings, which support nearly identical modes (though they interact with two sidewalls and are laterally

offset with respect to the microdisk modes). Moreover, our experimentally-demonstrated microrings already exhibit $Q \approx 2 \times 10^4$ (Fig. 6a). Strong coupling in these devices should then be achievable if this Q can be maintained when the microring diameter is shrunk to ≈ 2 μm, and if the quantum dot location with respect to the field maximum can be precisely set. Finally, we note that the refractive index contrast between GaAs and Si_3N_4 is large enough that we expect that other microcavity geometries, such as photonic crystals, may also be able to reach the strong coupling regime in our platform.

Supplementary Note 5 - Waveguide propagation loss estimate

To estimate propagation losses in our Si_3N_4 waveguides, we measure the transmission spectrum of a microring resonator fabricated on the same material using the same lithography and etching processes. The microring is formed by a waveguide with a $\approx$ 800 nm width and has a radius $R = 50$ μm. It is coupled evanescently to an 800 nm wide Si_3N_4 bus waveguide, which is in turn coupled-to with lensed optical fibers in the endfire configuration. The transmission spectrum shown in Supplementary Figure 4 is obtained by scanning the wavelength of a probing external-cavity tunable laser within the 940 nm band. The experimental data is fitted with the function

$$T(\omega) = \left| 1 - \frac{\kappa_e/2}{\kappa/2 + i\,(\omega - \omega_0)} \right|^2 , \tag{2}$$

where κ is the total cavity loss rate, κ_e is the external coupling rate between the cavity and the bus waveguide, ω_0 is the cavity angular frequency. Defining the total and coupling quality factors $Q = \omega/\kappa$ and $Q_e = \omega/\kappa_e$, the intrinsic quality factor Q_i, associated with the intrinsic loss rate κ_i of the microring, is $Q_i = \omega/\kappa_i = \left(Q^{-1} - Q_e^{-1}\right)^{-1}$. Fitting the spectrum in Supplementary Figure 4 gives $Q \approx 5 \times 10^5$, $Q_e \approx 3 \times 10^6$, $Q_i \approx 6 \times 10^5$. Such high quality factors are already comparable to those of similar Si_3N_4 microring devices recently used for demonstrating efficient on-chip wavelength conversion of single-photon level systems using the four-wave-mixing Bragg-scattering (FWM-BS) $\chi^{(3)}$ nonlinear optical process [7], and is sufficient for the realization of narrow-band on-chip filters for quantum dot emission, as demonstrated in [25]. For $\exp(-\alpha \cdot 2\pi R) \approx 1$, where α are the waveguide propagation losses, we may write [26] $\alpha \approx \lambda/(Q \cdot R \cdot \mathrm{FSR})$, where FSR=1.3 nm is the free-spectral range of our microring. With this, we estimate $\alpha \approx 1.1$ dB/cm. Such a loss figure is considerably lower then the lowest reported to date for GaAs waveguides used in single quantum dot investigations ($\approx$ 15 dB/cm in the 900 nm band in ref. 2, $\approx$ 17 dB/cm in the 1300 nm band [5]), and is lower than the $\approx$ 2.5 dB/cm-4 dB/cm observed in the 900 nm band in the SiN waveguides of ref. 19. It is worth mentioning that losses of the order of 1 dB/cm have only been reported for GaAs waveguides at 1330 nm [27] and 1550 nm wavelengths [28] (far away from the GaAs absoption edge at $\approx$ 800 nm), in purely passive ridge geometries supporting modes with weak lateral confinement. Weak confinement translates into large effective modal areas, which in turn lead to lesser light-matter interaction strengths - essentially geometries that are not ideal for coupling to single quantum dots.

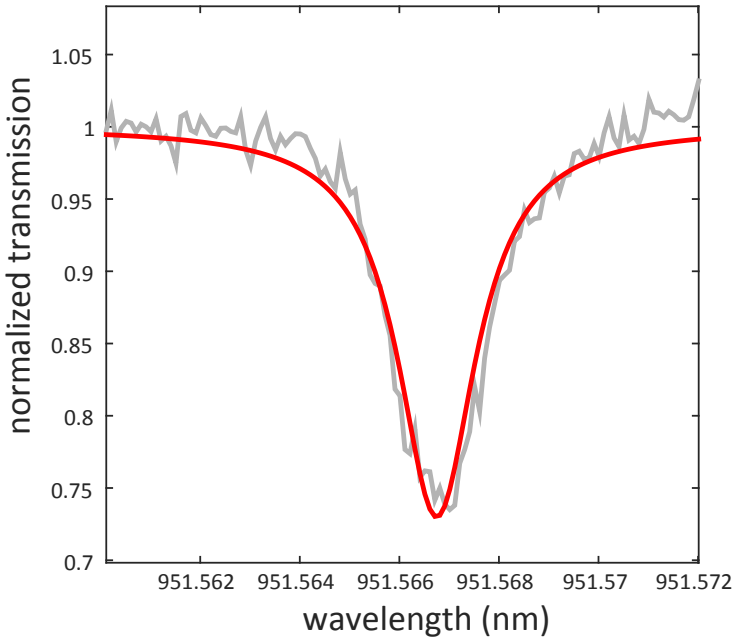

Supplementary Figure 4: **Si_3N_4 waveguide loss estimate**. Transmission spectrum for a waveguide-coupled Si_3N_4 microring resonator of 800 nm width and radius $R = 50$ μm. Gray curve: experimental data; red curve: fit. The fit gives a loaded $Q \approx 5 \times 10^5$, coupling $Q_e \approx 3 \times 10^6$, and intrinsic $Q_i \approx 6 \times 10^5$.

Supplementary Note 6 - Cryogenic measurement experimental setup

The setup used for low temperature cryogenic measurements is shown in Supplementary Figure 5. Samples were placed on a fixed mount inside a liquid Helium flow cryostat and cooled down ≈ 7 K. A microscope consisting of a long-working distance objective (20×, NA=0.4), beamsplitter (BS) and combination zoom lens / illuminator system mounted at the top cryostat window allowed devices on the sample surface to be imaged. An example image of a GaAs microring resonator device can be seen in the "sample imaging" box in the schematic of Supplementary Figure 5. Light from an external cavity tunable laser (ECDL) with center wavelength around 1060 nm was introduced into the objective via the beamsplitter, to produce a small (≈ 5 μm) spot that pumped QDs at select locations on the device under test. As discussed in the main text, photoluminescence from the QDs was coupled to Si_3N_4 waveguides, and collected at the cleaved edge of the chip with a lensed fiber. A nanopositiong stage stack placed inside the cryostat allowed the lensed fibers to be aligned to waveguide facets, as illustrated in Supplementary Figure 5.

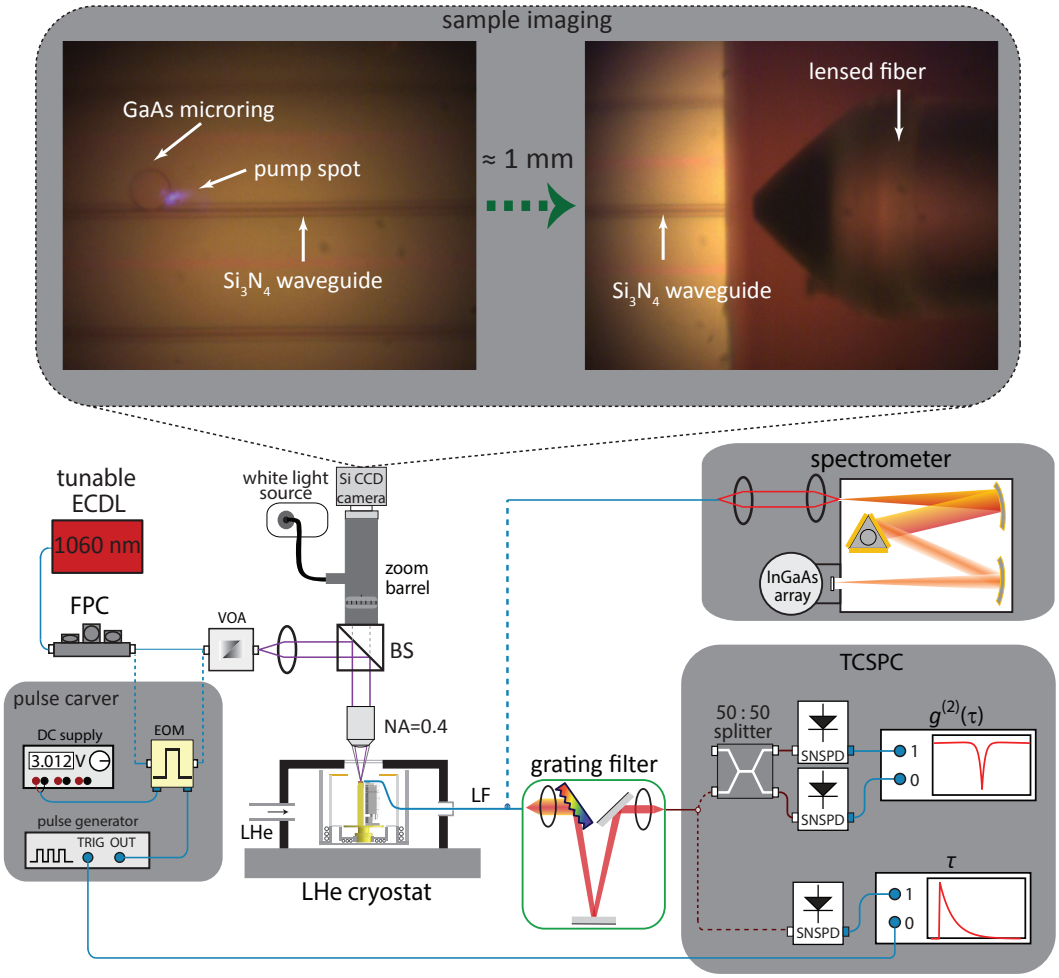

Supplementary Figure 5: **Cryogenic measurement setup**. Devices are tested inside a liquid Helium flow cryostat. A window at the top allows imaging of the sample, as shown in the "sample imaging" box. Devices are also pumped from the top with laser light (purple spot over portion of the GaAs microring resonator), and quantum dot photoluminescence is coupled into the Si_3N_4 waveguide. The emitted light travels ≈ 1 mm down the Si_3N_4 waveguide until the cleaved edge of the chip, where it is collected with a lensed fiber mounted to a nanopositioning stage inside the cryostat. The collected light can then be routed to a grating spectrometer, or filtered in a grating filter and then routed towards time-correlated single-photon counting measurements. Pulsed pumping can be achieved by modulating continuous-wave laser light with an electro-optic modulator. ECDL: external-cavity diode laser; FPC: fiber polarization controller; EOM: electro-optic modulator; BS: beamsplitter; VOA: variable optical attenuator. LF: lensed fiber. SNSPD: superconducting nanowire single-photon detector; TCSPC: time-correlated single-photon counting; CCD: charge-coupled device; LHe: liquid Helium

The collected photoluminescence was either be routed to a grating spectrometer equipped with a liquid-nitrogen cooled InGaAs photodiode array, or filtered through a ≈ 700 pm bandpass tunable grating filter and then routed towards our single-photon detection system for time-correlated single-photon counting (TCSPC) measurements of excited state lifetime and second-order correlations. For correlation measurements, we used a Hanbury-Brown and Twiss setup consisting of a fiber-based 50:50 beamsplitter connected to two amorphous WSi superconducting nanowire single-photon detectors (SNSPDs) [29]. Detector counts were correlated in a TCSPC unit.

For lifetime measurements, a 10 GHz lithium niobate electro-optic modulator (EOM) was used to produce a 80 MHz, ≈ 200 ps pulse train from the CW ECDL laser [30]. A fiber-based polarization controller (FPC) was used to control the polarization of the ECDL light going into the EOM, and a DC bias was applied to the EOM to maximize signal extinction. An electrical pulsed source was used to produce an 80 MHz train of ≈ 200 ps pulses of < 1 V peak amplitude, which was then amplified and used to drive the EOM modulator via its radio frequency (RF) port. A trigger signal from the pulse generator served as the reference channel in our TCSPC system. Supplementary Figure 6a shows a typical temporal profile for the pulses produced by the EOM, detected with an SNSPD. Pulse FWHM of ≈ 200 ps and > 20 dB extinction are observed. The pulsed electrical signal produced small satellite peaks that were imprinted in the optical signal, as indicated in Supplementary Figure 6a. Impulse response functions (IRFs) such as shown in Supplementary Figure 6a were used in decay lifetime fits as explained below, so that the effect of satellite peaks, though minimal, was accounted for.

To determine the time resolution of our detection system, we launched attenuated, few-picosecond pulses from a Ti:Sapphire mode-locked laser at 975 nm into the SNSPDs, to obtain the temporal trace in Supplementary Figure 6b. The peak can be well fitted with a Gaussian with standard deviation $\sigma = 129$ ps $\pm$ 0.04 ps (uncertainty is a 95 % least-squares fit confidence interval, corresponding to two standard deviations).

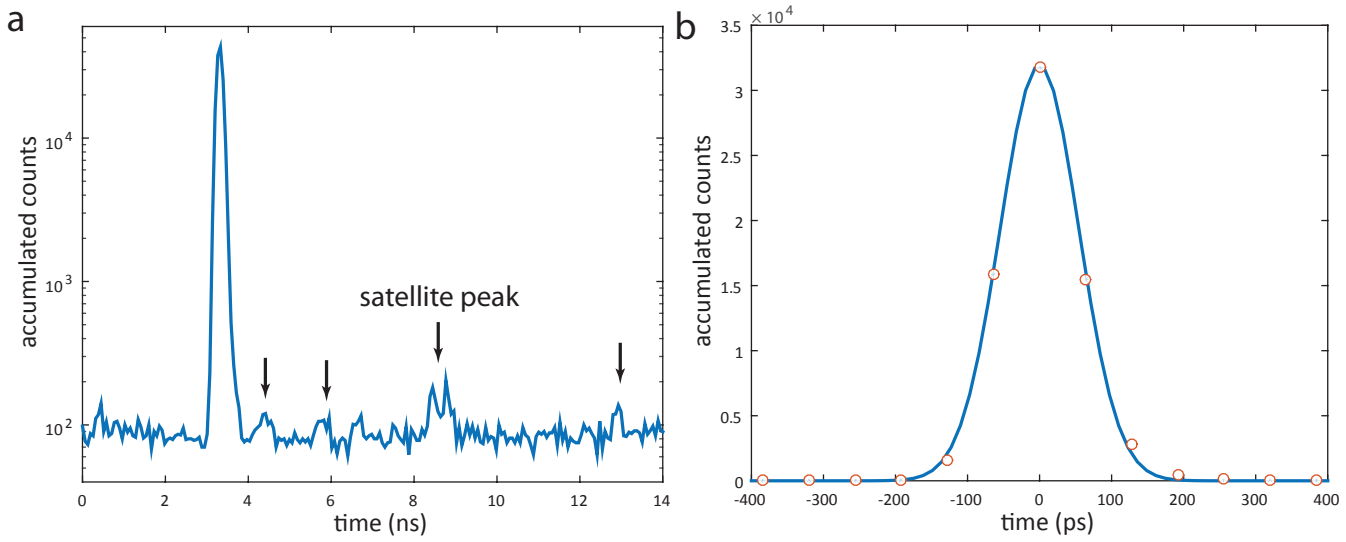

Supplementary Figure 6: **Impulse response functions**. **a**, Temporal profile of pulsed pump achieved with an electro-optic modulator (EOM). Satellite peaks due to an imperfect electrical driving signal are pinpointed with arrows. **b**, Impulse response of the SNSPD-based detection system, obtained with a ≈ ps pulsed Ti:Sapphire laser source.

Supplementary Note 7 - Purcell enhancement in the heterogeneous platform

Here we provide further information about the Purcell enhancement data and fits for the quantum dot in a microring resonator presented in Figs. 6d-6g of the main text. Supplementary Figures 7a and 7b respectively show lifetimes and corresponding decay component amplitudes for the fits, as a function of the detuning Δ. It is apparent that the fast lifetimes vary considerably, from $\approx$ 414 ps at $\Delta \approx -0.26$ nm to $\approx$ 263 ps at $\Delta \approx -0.07$ nm, then to $\approx$ 1.1 ns at $\Delta = 0.84$ nm. Slow lifetimes remain consistently above 1 ns. The fast decay contribution remains above 50 % for all detunings except $\Delta \approx 0.36$ nm, where a second exciton (X_2) is seen to couple to the same whispering-gallery mode in Fig. 6f. The contributions of the two excitons and the cavity to the detected signal in the lifetime measurements is estimated through fits to the emission spectra at each detuning, shown in Supplementary Figure 7c. The X_1 contribution is seen to be dominant everywhere (except $\Delta \approx 0.36$ nm). The X_2 contribution is maximized at $\Delta \approx 0.36$ nm, but remains below 0.015 everywhere. These results indicate that the fast lifetimes can be assigned to the X_1 exciton. Further supporting this assignment is the fact that the good quality of the $g^{(2)}(\tau)$ fit in Fig. 6e was achieved by including a Poissonian background equal to the cavity contribution in the PL spectrum fit of Fig. 6d. Uncertainties for $g^{(2)}(0)$, Δ and the X_1, X_2 and cavity PL contributions are 95 % fit confidence intervals (two standard deviations). Uncertainties for τ are single standard deviations from the exponential decay fit procedure.

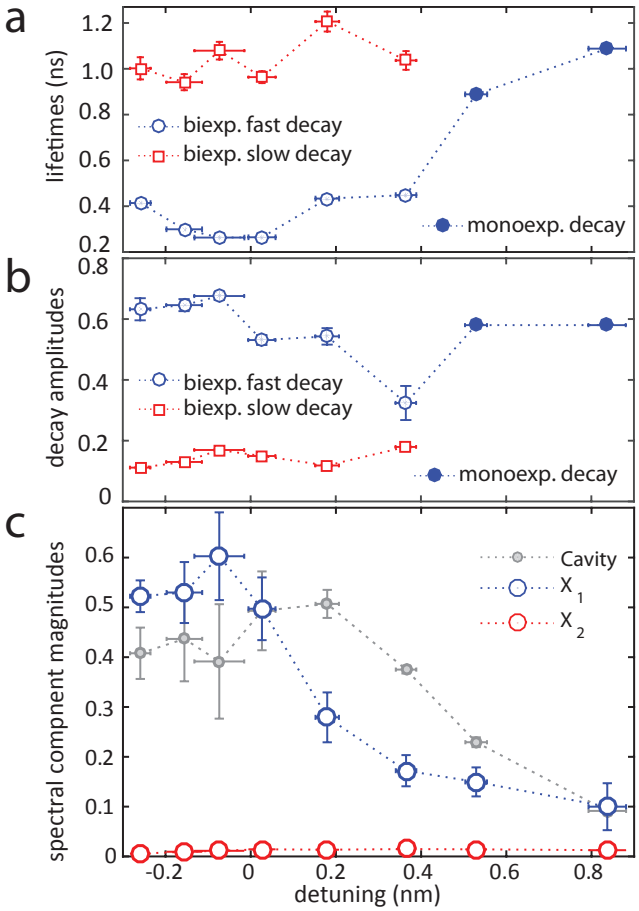

Supplementary Figure 7: **Lifetime and PL intensity fit results**. **a**, Decay lifetimes for the fits in Fig. 6f, as a function of the detuning Δ. Open blue circles and red squares are the fast and slow biexponential decay lifetimes, closed blue circles are the monoexponential decay lifetimes. **b**, Corresponding amplitudes for the different decay components. **c**, magnitudes of the X_1, X_2 and cavity Lorentzians used to fit the PL spectra in **f**, normalized to the sum of the integrated intensities of the three components before filtering. Uncertainties for Δ and the X_1, X_2 and cavity PL contributions are 95 % fit confidence intervals (two standard deviations). Uncertainties for τ are single standard deviations from the exponential decay fit procedure.

Supplementary Note 8 - Fisher information matrix

Variances for the estimated decay lifetime parameters in $\boldsymbol{\theta}$ can be obtained from the diagonal elements of the inverse of the Fisher Information Matrix $M(\theta)$ with

$$[M(\boldsymbol{\theta})]_{mn} = \mathbb{E}_{\boldsymbol{\theta}}\left[\frac{\partial \ln f_{\boldsymbol{\theta}}^{(k)}(Y^k)}{\partial \theta_m}\frac{\partial \ln f_{\boldsymbol{\theta}}^{(k)}(Y^k)}{\partial \theta_n}\right]. \tag{3}$$

Here, $\mathbb{E}_{\boldsymbol{\theta}}$ stands for expectation value, and $f_{\boldsymbol{\theta}}^{(k)}(y^k)$ is the probability mass function for the counts in each bin of the liftetime trace, which constitute a sequence of random variables with multinomial distibution [31]:

$$f_{\boldsymbol{\theta}}^{(k)}(y^k) = \frac{N!}{\prod_{i=1}^k y_i!}\prod_{i=1}^k p_i^{y_i}(\boldsymbol{\theta}),\ \sum_{i=1}^k y_i = N,\ \sum_{i=1}^k p_i(\boldsymbol{\theta}) = 1 \tag{4}$$

Noting that

$$\frac{\partial \ln f_{\boldsymbol{\theta}}^{(k)}(y^k)}{\partial \theta_m} = \sum_{i=1}^k \frac{y_i}{p_i(\boldsymbol{\theta})}\frac{\partial p_i(\boldsymbol{\theta})}{\partial \theta_m}, \tag{5}$$

we can write

$$\sum_{i=1}^k\sum_{j=1}^k \frac{\mathbb{E}_{\boldsymbol{\theta}}\left[Y_iY_j\right]}{p_i(\boldsymbol{\theta})p_j(\boldsymbol{\theta})}\frac{\partial p_i(\boldsymbol{\theta})}{\partial \theta_m}\frac{\partial p_j(\boldsymbol{\theta})}{\partial \theta_n} \tag{6}$$

Now

$$\mathbb{E}_{\boldsymbol{\theta}}\left[Y_iY_j\right] = \begin{cases} \mathrm{var}_{\boldsymbol{\theta}}\left[Y_i\right] + \left(\mathbb{E}_{\boldsymbol{\theta}}\left[Y_i\right]\right)^2 = (N^2-N)p_i^2(\boldsymbol{\theta}) + Np_i(\boldsymbol{\theta}) & \text{if } i=j, \\ \mathrm{COV}_{\boldsymbol{\theta}}\left[Y_i,Y_j\right] + \mathbb{E}_{\boldsymbol{\theta}}\left[Y_i\right]\mathbb{E}_{\boldsymbol{\theta}}\left[Y_j\right] = (N^2-N)p_i(\boldsymbol{\theta})p_j(\boldsymbol{\theta}) & \text{if } i\neq j, \end{cases} \tag{7}$$

where $\mathrm{var}_{\boldsymbol{\theta}}$ and $\mathrm{COV}_{\boldsymbol{\theta}}$ are the variance and the covariance operators with respect to $\boldsymbol{\theta}$, respectively. Substituting (7) into (6), it follows that

$$\begin{aligned}\mathbb{E}_{\boldsymbol{\theta}}\left[\frac{\partial \ln f_{\boldsymbol{\theta}}^{(k)}(Y^k)}{\partial \theta_m}\frac{\partial \ln f_{\boldsymbol{\theta}}^{(k)}(Y^k)}{\partial \theta_n}\right] =& \sum_{i=1}^k \frac{(N^2-N)p_i^2(\boldsymbol{\theta})y + Np_i(\boldsymbol{\theta})}{p_i^2(\boldsymbol{\theta})}\frac{\partial p_i(\boldsymbol{\theta})}{\partial \theta_m}\frac{\partial p_i(\boldsymbol{\theta})}{\partial \theta_n} \\ &+ \underbrace{\sum_{i=1}^k\sum_{j=1}^k}_{i\neq j}\frac{(N^2-N)p_i(\boldsymbol{\theta})p_j(\boldsymbol{\theta})y}{p_i(\boldsymbol{\theta})p_j(\boldsymbol{\theta})}\frac{\partial p_i(\boldsymbol{\theta})y}{\partial \theta_m}\frac{\partial p_j(\boldsymbol{\theta})}{\partial \theta_n}\end{aligned} \tag{8}$$

The first summation can be written as

$$\sum_{i=1}^k \frac{(N^2-N)p_i^2(\boldsymbol{\theta}) + Np_i(\boldsymbol{\theta})}{p_i^2(\boldsymbol{\theta})}\frac{\partial p_i(\boldsymbol{\theta})}{\partial \theta_m}\frac{\partial p_i(\boldsymbol{\theta})}{\partial \theta_n} = (N^2-N)\sum_{i=1}^k \frac{\partial p_i(\boldsymbol{\theta})y}{\partial \theta_m}\frac{\partial p_i(\boldsymbol{\theta})}{\partial \theta_n} + N\sum_{i=1}^k \frac{1}{p_i(\boldsymbol{\theta})}\frac{\partial p_i(\boldsymbol{\theta})y}{\partial \theta_m}\frac{\partial p_i(\boldsymbol{\theta})}{\partial \theta_n}. \tag{9}$$

The second summation can be written as

$$\underbrace{\sum_{i=1}^k\sum_{j=1}^k}_{i\neq j}\frac{(N^2-N)p_i(\boldsymbol{\theta})p_j(\boldsymbol{\theta})}{p_i(\boldsymbol{\theta})p_j(\boldsymbol{\theta})}\frac{\partial p_i(\boldsymbol{\theta})}{\partial \theta_m}\frac{\partial p_j(\boldsymbol{\theta})}{\partial \theta_n} = (N^2-N)\underbrace{\sum_{i=1}^k\sum_{j=1}^k}_{i\neq j}\frac{\partial p_i(\boldsymbol{\theta})}{\partial \theta_m}\frac{\partial p_j(\boldsymbol{\theta})y}{\partial \theta_n} \tag{10}$$

Substituting (9) and (10) into (8), it follows that

$$\mathbb{E}_{\boldsymbol{\theta}}\left[\frac{\partial \ln f_{\boldsymbol{\theta}}^{(k)}(Y^k)}{\partial \theta_m}\frac{\partial \ln f_{\boldsymbol{\theta}}^{(k)}(Y^k)}{\partial \theta_n}\right] = (N^2-N)\sum_{i=1}^k\sum_{j=1}^k \frac{\partial p_i(\boldsymbol{\theta})}{\partial \theta_m}\frac{\partial p_j(\boldsymbol{\theta})}{\partial \theta_n} + N\sum_{i=1}^k \frac{1}{p_i(\boldsymbol{\theta})}\frac{\partial p_i(\boldsymbol{\theta})y}{\partial \theta_m}\frac{\partial p_i(\boldsymbol{\theta})}{\partial \theta_n}. \tag{11}$$

Noting that

$$\sum_{i=1}^{k}\sum_{j=1}^{k}\frac{\partial p_i(\boldsymbol{\theta})}{\partial\theta_m}\frac{\partial p_j(\boldsymbol{\theta})}{\partial\theta_n}=\sum_{i=1}^{k}\frac{\partial p_i(\boldsymbol{\theta})y}{\partial\theta_m}\sum_{j=1}^{k}\frac{\partial p_j(\boldsymbol{\theta})}{\partial\theta_n}=\frac{\partial\left(\sum_{i=1}^{k}p_i(\boldsymbol{\theta})\right)}{\partial\theta_m}\frac{\partial\left(\sum_{j=1}^{k}p_j(\boldsymbol{\theta})\right)}{\partial\theta_n}=\frac{\partial(1)}{\partial\theta_m}\frac{\partial(1)}{\partial\theta_n}=0, \tag{12}$$

it follows that

$$\mathbb{E}_{\boldsymbol{\theta}}\left[\frac{\partial\ln f_{\boldsymbol{\theta}}^{(k)}(Y^k)}{\partial\theta_m}\frac{\partial\ln f_{\boldsymbol{\theta}}^{(k)}(Y^k)}{\partial\theta_n}\right]=N\sum_{i=1}^{k}\frac{1}{p_i(\boldsymbol{\theta})y}\frac{\partial p_i(\boldsymbol{\theta})}{\partial\theta_m}\frac{\partial p_i(\boldsymbol{\theta})}{\partial\theta_n}. \tag{13}$$

We next define

$$p_i(\tau)=e^{-ir/k}\frac{e^{\frac{r}{k}}-1}{1-e^{-r}},\ r\triangleq\frac{i\cdot\Delta t}{\tau} \tag{14}$$

$$\frac{\partial p_i(\tau)}{\partial\tau}=\frac{-r}{\tau}p_i(\tau)\left(-\frac{i}{k}+\frac{e^{r/k}}{(e^{r/k}-1)k}-\frac{e^{-r}}{1-e^{-r}}\right). \tag{15}$$

For a monoexponential decay when a portion b of the signal is due to background emission,

$$p_i(\tau,b)=\frac{b}{k}+(1-b)p_i(\tau) \tag{16}$$

The Fisher matrix in this case can be computed with eq.(13) and

$$\frac{\partial p_i(\tau,b)}{\partial b}=\frac{1}{k}-p_i(\tau) \tag{17}$$

$$\frac{\partial p_i(\tau,b)}{\partial\tau}=(1-b)\frac{-r}{\tau}p_i(\tau)\left(-\frac{i}{k}+\frac{e^{r/k}}{(e^{r/k}-1)k}-\frac{e^{-r}}{1-e^{-r}}\right) \tag{18}$$

For biexponential decay with a background, let $\tau\triangleq(\tau_1,\tau_2)^T$. Then $p_i(\tau,a,b)$ (where a is the contribution of the first exponential decay) may be expressed as

$$p_i(\tau,b,a)=\frac{b}{k}+(1-b)\left[ap_i(\tau_1)+(1-a)p_i(\tau_2)\right] \tag{19}$$

The Fisher matrix in this case can be computed with eq.(13) and

$$\frac{\partial p_i(\tau,b,a)}{\partial b}=\frac{1}{k}-\left[ap_i(\tau_1)+(1-a)p_i(\tau_2)\right] \tag{20}$$

$$\frac{\partial p_i(\tau,b,a)}{\partial\tau_1}=a(1-b)\frac{\partial p_i(\tau_1)}{\partial\tau_1} \tag{21}$$

$$\frac{\partial p_i(\tau,b,a)}{\partial\tau_2}=(1-a)(1-b)\frac{\partial p_i(\tau_2)}{\partial\tau_2} \tag{22}$$

$$\frac{\partial p_i(\tau,b,a)}{\partial a}=(1-b)\left(p_i(\tau_1)-p_i(\tau_2)\right). \tag{23}$$

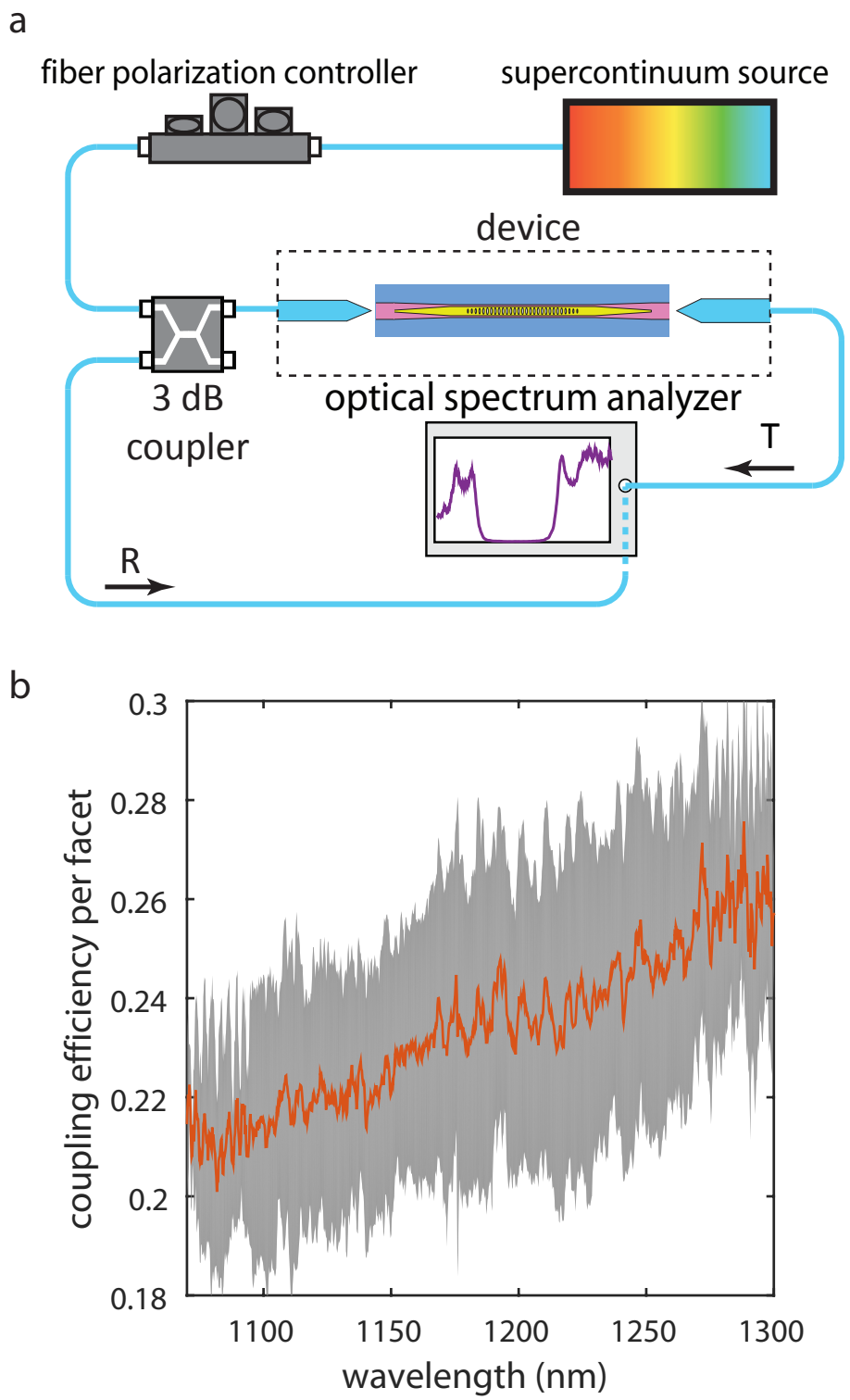

Supplementary Figure 8: **Photonic characterization setup**. **a**, Experimental setup for passive, endfire coupling measurement of transmitted (T) and reflected (R) power. **b**, Measured coupling efficiency per facet (including fiber-to-waveguide coupling and propagation losses in the waveguide between the facet and a GaAs device) as a function of wavelength. The red curve and grey area are the mean value and standard deviation over three measured waveguides.

Supplementary References

[1] C. P. Dietrich, A. Fiore, M. G. Thompson, M. Kamp, and S. Höfling, "GaAs integrated quantum photonics: Towards compact and multi-functional quantum photonic integrated circuits," Laser & Photonics Reviews **10**, 870-894 (2016).

[2] K. D. Jöns, U. Rengstl, M. Oster, F. Hargart, M. Heldmaier, S. Bounouar, S. M. Ulrich, M. Jetter, and P. Michler, "Monolithic on-chip integration of semiconductor waveguides, beamsplitters and single-photon sources," Journal of Physics D: Applied Physics **48**, 085 101 (2015).

[3] G. Reithmaier, M. Kaniber, F. Flassig, S. Lichtmannecker, K. Müller, A. Andrejew, J. Vučković, R. Gross, and J. J. Finley, "On-Chip Generation, Routing, and Detection of Resonance Fluorescence," Nano Lett. **15**, 5208–5213 (2015).

[4] N. Prtljaga, R. J. Coles, J. O'Hara, B. Royall, E. Clarke, A. M. Fox, and M. S. Skolnick, "Monolithic integration of a quantum emitter with a compact on-chip beam-splitter," Applied Physics Letters **104**, 231 107 (2014).

[5] S. F. poor, T. B. Hoang, L. Midolo, C. P. Dietrich, L. H. Li, E. H. Linfield, J. F. P. Schouwenberg, T. Xia, F. M. Pagliano, F. W. M. v. Otten, and A. Fiore, "Efficient coupling of single photons to ridge-waveguide photonic integrated circuits," Applied Physics Letters **102**, 131 105 (2013).

[6] M. Davanço and K. Srinivasan, "Fiber-coupled semiconductor waveguides as an efficient optical interface to a single quantum dipole," Opt. Lett. **34**, 2542–2544 (2009).

[7] Q. Li, M. Davanço, and K. Srinivasan, "Efficient and low-noise single-photon-level frequency conversion interfaces using silicon nanophotonics," Nature Photonics **10**, 406–414 (2016).

[8] T. Shoji, T. Tsuchizawa, T. Watanabe, K. Yamada, and H. Morita, "Low loss mode size converter from 0.3 μm square Si wire waveguides to singlemode fibres," Electronics Letters **38**, 1669–1670 (2002).

[9] T. Tsuchizawa, K. Yamada, H. Fukuda, T. Watanabe, J.-i. Takahashi, M. Takahashi, T. Shoji, E. Tamechika, S. Itabashi, and H. Morita, "Microphotonics devices based on silicon microfabrication technology," IEEE Journal of Selected Topics in Quantum Electronics **11**, 232–240 (2005).

[10] X. Sun and A. Yariv, "Engineering supermode silicon/III-V hybrid waveguides for laser oscillation," JOSA B **25**, 923–926 (2008).

[11] M. Davanço and K. Srinivasan, "Efficient spectroscopy of single embedded emitters using optical fiber taper waveguides," Optics Express **17**, 10 542–10 563 (2009).

[12] A. W. Fang, H. Park, Y.-h. Kuo, R. Jones, O. Cohen, D. Liang, O. Raday, M. N. Sysak, M. J. Paniccia, and J. E. Bowers, "Hybrid silicon evanescent devices," Materials Today **10**, 28–35 (2007).

[13] J. E. Bowers, T. Komljenovic, M. Davenport, J. Hulme, A. Y. Liu, C. T. Santis, A. Spott, S. Srinivasan, E. J. Stanton, and C. Zhang, "Recent advances in silicon photonic integrated circuits," p. 977402 (2016).

[14] B. Rigal, C. Jarlov, P. Gallo, B. Dwir, A. Rudra, M. Calic, and E. Kapon, "Site-controlled quantum dots coupled to a photonic crystal molecule," Applied Physics Letters **107**, 141 103 (2015).

[15] C. Schneider, A. Huggenberger, M. Gschrey, P. Gold, S. Rodt, A. Forchel, S. Reitzenstein, S. Höfling, and M. Kamp, "In(Ga)As/GaAs site-controlled quantum dots with tailored morphology and high optical quality," physica status solidi (a) **209**, 2379–2386 (2012).

[16] M. Helfrich, P. Schroth, D. Grigoriev, S. Lazarev, R. Felici, T. Slobodskyy, T. Baumbach, and D. M. Schaadt, "Growth and characterization of site-selective quantum dots," physica status solidi (a) **209**, 2387–2401 (2012).

[17] L. Sapienza, M. Davanço, A. Badolato, and K. Srinivasan, "Nanoscale optical positioning of single quantum dots for bright and pure single-photon emission," Nature Communications **6**, 7833 (2015).

[18] J. Liu, M. I. Davanco, L. Sapienza, K. Konthasinghe, J. V. D. M. Cardoso, J. D. Song, A. Badolato, and K. Srinivasan, "Cryogenic photoluminescence imaging system for nanoscale positioning of single quantum emitters," Review of Scientific Instruments **88**, 023 116 (2017).

[19] I. E. Zadeh, A. W. Elshaari, K. D. Jöns, A. Fognini, D. Dalacu, P. J. Poole, M. E. Reimer, and V. Zwiller, "Deterministic Integration of Single Photon Sources in Silicon Based Photonic Circuits," Nano Lett. **16**, 2289–2294 (2016).

[20] S. L. Mouradian, T. Schröder, C. B. Poitras, L. Li, J. Goldstein, E. H. Chen, M. Walsh, J. Cardenas, M. L. Markham, D. J. Twitchen, M. Lipson, and D. Englund, "Scalable Integration of Long-Lived Quantum Memories into a Photonic Circuit," Phys. Rev. X **5**, 031 009 (2015).

[21] E. Murray, D. J. P. Ellis, T. Meany, F. F. Floether, J. P. Lee, J. P. Griffiths, G. A. C. Jones, I. Farrer, D. A. Ritchie, A. J. Bennett, and A. J. Shields, "Quantum photonics hybrid integration platform," Applied Physics Letters **107**, 171 108 (2015).

[22] E. Bermúdez-Ureña, C. Gonzalez-Ballestero, M. Geiselmann, R. Marty, I. P. Radko, T. Holmgaard, Y. Alaverdyan, E. Moreno, F. J. García-Vidal, S. I. Bozhevolnyi, and R. Quidant, "Coupling of individual quantum emitters to channel plasmons," Nature Communications **6**, 7883 (2015).

[23] The identification of any commercial product or trade name is used to foster understanding. Such identification does not imply recommendation or endorsement or by the National Institute of Standards and Technology, nor does it imply that the materials or equipment identified are necessarily the best available for the purpose.

[24] K. Srinivasan and O. Painter, "Linear and nonlinear optical spectroscopy of a strongly coupled microdisk-quantum dot system," Nature **450**, 862–865 (2007).

[25] A. W. Elshaari, I. E. Zadeh, A. Fognini, M. E. Reimer, D. Dalacu, P. J. Poole, V. Zwiller, and K. D. Jöns, "On-Chip Single-Photon Sifter." Pre-print at https://arxiv.org/abs/1611.03245v3 (2016).

[26] K. Luke, A. Dutt, C. B. Poitras, and M. Lipson, "Overcoming Si_3N_4 film stress limitations for high quality factor ring resonators," Optics Express **21**, 22 829–22 833 (2013).

[27] H. Inoue, K. Hiruma, K. Ishida, T. Asai, and H. Matsumura, "Low loss GaAs optical waveguides," IEEE Transactions on Electron Devices **32**, 2662–2668 (1985).

[28] J. Wang, A. Santamato, P. Jiang, D. Bonneau, E. Engin, J. W. Silverstone, M. Lermer, J. Beetz, M. Kamp, S. Höfling, M. G. Tanner, C. M. Natarajan, R. H. Hadfield, S. N. Dorenbos, V. Zwiller, J. L. O'Brien, and M. G. Thompson, "Gallium arsenide (GaAs) quantum photonic waveguide circuits," Optics Communications **327**, 49–55 (2014).

[29] F. Marsili, V. B. Verma, J. A. Stern, S. Harrington, A. E. Lita, T. Gerrits, I. Vayshenker, B. Baek, M. D. Shaw, R. P. Mirin, and S. W. Nam, "Detecting single infrared photons with 93% system efficiency," Nature Photonics **7**, 210–214 (2013).

[30] A. C. Dada, T. S. Santana, R. N. E. Malein, A. Koutroumanis, Y. Ma, J. M. Zajac, J. Y. Lim, J. D. Song, and B. D. Gerardot, "Indistinguishable single photons with flexible electronic triggering," Optica **3**, 493–498 (2016).

[31] M. Köllner and J. Wolfrum, "How many photons are necessary for fluorescence-lifetime measurements?" Chemical Physics Letters **200**, 199–204 (1992).